CZECH TECHNICAL UNIVERSITY IN PRAGUE

Faculty of Biomedical Engineering

Department of Natural Sciences

Time-of-Flight analysis of reaction products for laser-induced proton-boron fusion cancer therapy

Master's thesis

Study program: Biomedical and clinical technology

Study branch: Instruments and Methods for Biomedicine

Supervisor: Dr. Valentina Scuderi

Consultant: Ing. Petr Brůža, Ph.D.

Bc. Viktória Fedorová

Kladno 2017

DECLARATION

I declare that I elaborated the master thesis **Time-of-Flight analysis of reaction products for laser-induced proton-boron fusion cancer therapy** independently and only with cited sources and literature referred in the end of the thesis.

Prohlašuji, že jsem diplomovou práci s názvem **Time-of-Flight analýza reakčních produktů pro laserem buzenou proton-borovou fúzní terapii nádorů** vypracovala samostatně a použila k tomu úplný výčet citací použitých pramenů, které uvádím v seznamu přiloženém k diplomové práci.

Nemám závažný důvod proti užití tohoto školního díla ve smyslu § 60 zákona č. 121/2000 Sb., o právu autorském, o právech souvisejících s právem autorským a o změně některých zákonů (autorský zákon), ve znění pozdějších předpisů.

In Kladno 19. 5. 2017

…...……...……...

Bc. Viktória Fedorová

ACKNOWLEDGMENTS

Here I would like to thank my supervisor Dr. Valentina Scuderi for her patience, valuable advices and optimism during the last days of writing. My deepest gratitude goes also to amazing Giuliana Milluzzo for her help and smart explanations that make this thesis even better. I want to also thank to all my family, friends and especially Ján Juranko, who have been supporting me during this two-year journey.

I'd like to kindly thank everyone that has participated at PALS experiment and PALS staff for making this thesis possible. Special thanks go to Giada Petringa for providing me the results of CR-39 detectors analysis. I want also thank to INFN-LNS for giving me the opportunity to spend some quality time in Catania during the analysis.

This work has been performed within the ELIMED activities supported by the V committee of INFN (Italian Institute for Nuclear Physics), by the MIUR (Italian Ministry of Education, Research and University), by the ELI-Beamlines Contract no S14-187 under CZ.02.1.01/0.0/0.0/15 − 008/0000162 through the European Regional Development Fund, by the Ministry of Education, Youth and Sports of the Czech Republic (National Program of Sustainability II Project No. LQ1606) and by the EPSRC (grant n. EP/K022415/1).

Název diplomové práce:

Time-of-Flight analýza reakčních produktů pro laserem buzenou proton-bórovou fúzní terapii nádorů

Abstrakt:

Tato diplomová práce je zaměřená na diagnostiku svazku generovaného interakcí laserového svazku se speciálně vyvinutým terčem dopovaném bórem a vodíkem pomocí metody měření doby letu. Proton-bórová fúzní reakce, která během interakce nastává, může být potenciálně využitá jako efektivnější varianta současné protonové terapie. Tato reakce produkuje alfa-částice, které dokážou způsobit větší poškození DNA nádorových buněk než samy protony. Hlavním cílem práce je charakterizovat svazek částic produkovaných při laserem-indukované proton-bórové fúzi co se týče energie, úhlové distribuce a toku. Za tímto účelem byl provedený experiment v laserové laboratoři PALS v Praze za použití silikon-karbidových a diamantových detektorů. Tato práce diskutuje výsledky analýzy Time-of-Flight spekter naměřených během experimentu.

Klíčová slova:

Metoda měření doby letu, Proton-Bórová fúzní terapie, diagnostika laserem urychlovaných svazků, Silikon-karbidový detektor, diamantový detektor,

Master Thesis title:

Time-of-Flight analysis of reaction products for laser-induced proton-boron fusion cancer therapy

Abstract:

This thesis is focused on the Time-of-Flight diagnostics of the beam generated via laser-target interaction using specially developed boron-enriched target. The proton-boron fusion reaction that occurs during the interaction can be potentially used as a more efficient way for the proton therapy cancer treatment. Such reaction produces alpha particles that will cause more dramatic damage to the DNA of tumorous cells than protons in the regular proton therapy. The main goal of this work is to characterize the beam of particles produced during the laser-induced proton-boron nuclear fusion in terms of energy, angular distribution and fluence. For this purpose, an experiment at Prague Asterix Laser System (PALS) laboratory has been performed using Silicon Carbide (SiC) and diamond detectors as the most suitable diagnostics tools. This work will report the results of the analysis of the Time-of-Flight data obtained during the experiment.

Key words:

Time-of-Fight diagnostics, Proton-Boron fusion therapy, laser-driven ion beam diagnostics, SiC detector, diamond detector.

Contents

List of abbreviations

Abbreviation	Meaning
TOF	Time of Flight
SiC	Silicon Carbide detector
LET	Linear Energy Transfer
RBE	Relative Biological Effectiveness
OER	Oxygen Enhancement Ratio
PBFT	Proton-Boron Fusion Therapy
BUR	Boron Uptake Region
TNSA	Target Normal Sheath Acceleration
ELI	Extreme Light Infrastructure
ELIMAIA	ELI Multidisciplinary Applications of laser-Ion Acceleration
PMQs	Permanent Magnetic Quadrupoles
ESS	Energy Selector System
PALS	Prague Asterix Laser System
TP	Thompson Parabola spectrometer
SiH-B	Silicon target doped with boron and hydrogen atoms
SiH-B+PR	Silicon target doped with boron and hydrogen atoms with additional photo resistive layer

Introduction

The increase of the laser intensities opened the field to the ion acceleration by laser-plasma interaction. Their potential of producing high energetic particles (in range of several hundreds of MeV [1]) makes the high-power lasers a promising alternative to the conventional radio-frequency accelerators. Nowadays used ion accelerators for cancer treatment, such as cyclotron or synchrotron, are very huge, complex and expensive machines that often limit their worldwide spread. For this reason, a huge interest of the scientific community has been recently addressed to the study of high power laser interaction with the matter as an alternative ion source for multidisciplinary applications, including the medical one.

However, optically accelerated beam exhibits characteristics extremely different from the conventionally accelerated ones, such as wide energy spread and angular divergence, high peak current and high dose-rates in a single pulse [2]. Thus, in order to deliver the beam with stable parameters suitable for multidisciplinary applications, the development of the transport, selection and diagnostics devices is crucial. For this purpose, the ELIMAIA beamline will be installed at the ELI-Beamlines facility in Czech Republic. The diagnostics system plays a key role in on-line characterization of the beam parameters in terms of particles species, energy and fluence. When considering the peculiar features of the optically accelerated beam, Silicon Carbide (SiC) and diamond detectors have shown to be the most appropriate detectors for this purpose. Their interesting characteristics, such as radiation hardness, low capacitance and good time resolution, allow performing measurement using the Time-of-Flight technique.

This thesis is focused on the diagnostics of the alpha particles produced during the laser-induced proton-boron fusion by using SiC and diamond detectors. High-energetic alpha particles are produced in the fusion reaction between proton and boron. Proton-boron fusion reaction has also a promising potential applicability in the proton therapy since the efficiency of the treatment could be increased by the injection of boron compound to the tumor area. When irradiating this region with the proton beam used in

conventional proton therapy, alpha particles are produced within the tumor volume resulting in higher delivered dose.

In order to obtain the alpha particles from the laser-plasma interaction, specially developed boron doped hydrogen-enriched targets were used to trigger the reaction by accelerated protons. The experimental campaign was performed at PALS laboratory in Prague and its main aim was to maximize the alpha particle yield with using moderate laser intensities and measure the alpha particle angular distribution.

First chapter focuses on the description of the interaction of the heavy charged particles with matter, which offers dose deposition profile suitable for the cancer therapy. The advantages of the proton therapy in comparison conventional radiotherapy are also discussed. In the end of the chapter, proton-boron fusion reaction is described as well as its potential application in hadron therapy field.

The second chapter contains the principle of the laser-driven ion beam generation, their characteristics and their comparison with conventionally accelerated beams. It is also dedicated to the description of the ELIMAIA beamline, mainly to the diagnostics system. In this chapter, SiC and diamond detectors and their working principles are also described.

The third chapter is dedicated to the experimental setup of the campaign performed at PALS. The description of targets and detectors used, as well as the principle of Time-of-Flight analysis procedure, is included.

The fourth chapter reviews the results of the analysis and compares them with the results from the other detectors used during the experiment.

Final chapter is dedicated to the discussion of obtained results and concludes the thesis.

Goals of the thesis

The main aim of this thesis is the Time-of-Flight (TOF) diagnostics of the laser-driven ion beam and reaction products emitted in the fusion reaction experiment performed at PALS. This experimental campaign was focused on the production of high-energetic alpha particles by using specially developed targets doped with boron and hydrogen atoms. Similar experimental campaign was performed by the same research group where a high yield of alpha particles were produced (around 10^9 per steradians) using a laser pulse with moderate power (2 TW) and intensity (3×10^{16} W/cm^2) [35]. Using such laser parameters to obtain high number of alpha particles allows its production with longer laser pulse, which does not imply special laser techniques for compression pulses, so the less sophisticated and cheaper laser system might be used. Enhancing the number of particles with the specially developed target geometry might allow the generation of new brilliant radiation sources.

The thesis author has actively participated to the preparation and to the experimental campaign which main aim was to maximize the alpha yield by using the targets with even higher concentration of doped elements than the ones used in previous campaign. The main task of the thesis was to analyze the data from the TOF detectors used in this experiment by performing a script written in MATLAB software, as well as the interpretation of the results and the comparison with results from other detector employed in the experiment. As a result, the produced alpha particles will be characterized in terms of energy, fluence and mainly angular distribution, which was not measured in previous experiment.

1. State of the art

Nowadays, radiotherapy plays an important role in the cancer treatment, which is after surgery the most frequently and successfully applied form of therapy. The key problem in radiotherapy is the delivery of the highest dose needed to kill the cancer cells to the tumor region in such way that minimal damage will occur within the surrounding healthy tissue. The proton and heavier ion beams offer optimum dose deposition within the tumor tissue in comparison with nowadays mostly used conventional photon therapy [3]. Dose distribution of these particles (also known as heavy charged particles) stems from the nature of their interaction with the matter. This chapter describes the principle and advantages of the proton therapy and introduces the use of proton-boron nuclear reaction as the more efficient way of destroying cancerous cell within the therapy.

1.1. Interaction of heavy charged particle with matter

Proton and alpha particles, as more in general light ions, belong to the group referred as heavy charged particles. In particular, when passing through the matter, heavy charged particle interacts with the atoms of the material resulting in an energy loss and a deflection from its incident direction primarily as the result of the following two processes:

- non-elastic collisions with electrons of the material atoms,
- elastic scattering by atom nuclei.

From these two processes, the non-elastic collisions are solely responsible for the energy loss of the heavy charged particle in the material. The heavy charged particle interacts with the orbital electrons in its vicinity via Coulomb interactions leading to two possible effects:

- *excitation* – the electron is transferred to a higher energetic state within the absorber atom,
- *ionization* – the electron is completely removed from the atom.

As a result of such encounter, heavy charged particle loses certain amount of energy reflected by decreased velocity. The maximum energy that can be transferred from heavy charged particle of mass *m* with kinetic energy *E* to an electron of mass m_0 in one collision is $4Em_0/m$ [4]. Since the mass of the heavy particle (e.g. proton) is much higher than mass of the electron (approximately 10^4 higher), the heavy particle loses just a small fraction of its total energy within the collision without any significant deflection from its incident direction resulting in a quite straight track. For this reason, particle of certain energy can be characterized by a definite range depending on the absorber material.

1.1.1. Bragg peak

The energy loss of the heavy charged particle $\mathrm{d}E$ within the absorber material along the corresponding path $\mathrm{d}x$ is referred as *linear stopping power S*, expressed as:

$$S = -\frac{\mathrm{d}E}{\mathrm{d}x} \tag{1.1}$$

Since the stopping power depends on the type of the particle, its mass and charge state as well as the absorber parameters, the stopping power can be described using expression (1.2) also known as the Bethe formula [5]:

$$-\frac{\mathrm{d}E}{\mathrm{d}x} = \frac{4\pi e^4 z^2}{m_0 v^2} NZ \left[\ln\frac{2m_0 v^2}{I} - \ln(1-\beta^2) - \beta^2 - \frac{C}{Z} - \frac{\delta}{2}\right] \tag{1.2}$$

where *e* is the elementary charge, *z* is the charge of the particle, *N* and *Z* are respectively the density and atomic number of the absorber atoms, *I* is the average ionization potential experimentally ascertained for each element. Coefficient β represents the ratio of particle's velocity to the speed of light $\beta = \frac{v}{c}$. The terms C/Z and $\delta/2$ represents the shell and the density corrections for the energy loss in case of very high or very low energetic particles.

By plotting the stopping power values versus the charged particle path length it is possible to define the functionality known as *Bragg curve* named after the Australian physicist Sir William Henry Bragg who discovered this phenomenon [6], see Figure 1.

The significant energy loss drop to zero corresponds to the path length where the particles picked up enough electrons to become a neutral atom and their track ends.

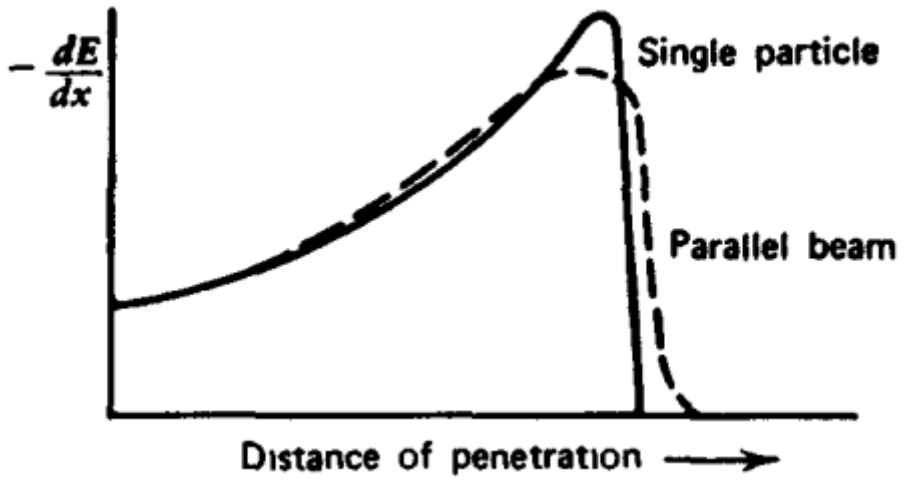

Figure 1: The energy loss of heavy charged particle along its track - Bragg curve [4]

As one can see in Figure 1, there is a difference between the stopping power of a single particle and a beam of the particles with the same initial energy. Indeed, since inelastic collisions happen randomly and occur with a certain probability, the energy loss is a statistical process. For this reason, an energy spread occurs when different particles with the same energy penetrate a given material and this effect is called *energy straggling*. Same stochastic factors result in different path length for each particle causing a *range straggling*. In particular, the *range* defines the distance in the absorber beyond no particle of certain energy will penetrate. Theoretically, it is possible to calculate the energy range of a particle with energy T_0 by integrating the stopping power formula (1.1):

$$S(T_0) = \int_0^{T_0} \left(\frac{\mathrm{d}E}{\mathrm{d}x}\right)^{-1} \mathrm{d}E \tag{1.3}$$

However, according to the straggling effect, the range cannot be exactly defined. For this purpose, the *mean range* R_m is defined as a thickness of the absorber that reduces the number of particles to 50%. Another possible calculation present in the literature is

the use of *extrapolated range* R_e which could be obtained by extrapolating the linear part of the end of the transmission curve to zero [4]. The Figure 2 shows the ratio of number of transmitted particles to number of incoming particles versus absorber thickness *t* with the illustration of the R_e and R_m evaluation.

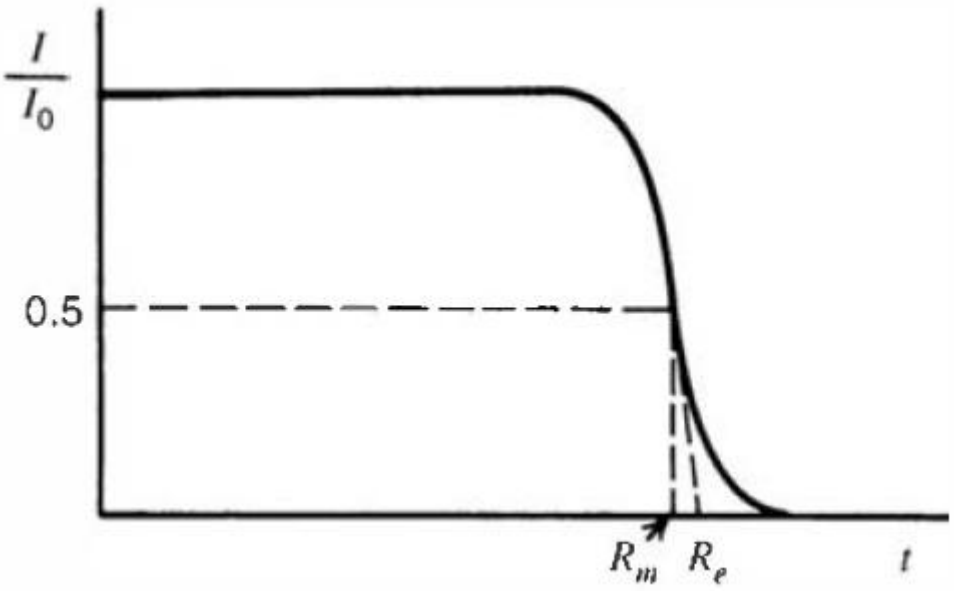

Figure 2: This plot shows the ratio of number of transmitted particles to number of incoming ones along the path length within the absorber. The illustration of range calculations is depicted as well. [4]

1.1.2. Biological effects

The biological effects caused by the passage of heavy charged particles through the human tissue strongly depends on the type of the particles as it is a function of the *linear energy transfer* (LET). The LET is defined as the energy locally deposited to the medium d*E* per unit path length d*l*:

$$LET = \frac{\mathrm{d}E}{\mathrm{d}l} \tag{1.4}$$

For most purposes LET is the same as stopping power, equation (1.1). The only difference is the emission of bremsstrahlung generally escaping from the region of the particle path which is not included in LET calculation [5]. Typically, particles can be

divided into two groups according to their LET: low-LET (electrons and photons) and high-LET (α-particles, ions and neutrons) particles.

Quantity of radiation received by an object is measured by several different units [5]. The most relevant quantity for discussing the effects of irradiation is the *absorbed dose*. It is a quantity which measures the total energy absorbed per unit mass. However, it should be noted that absorbed dose gives no indication of the rate at which the irradiation occurred or specify the type of radiation.

In order to define the biological damage caused by a specific type of radiation, the *relative biological effectiveness* (RBE) is usually defined. The RBE compares the efficiency of different kinds of radiation producing the same biological effect as a reference radiation, typically photon. The RBE is defined as follow [3]:

$$RBE = \frac{D_{ref}}{D_{ion}} \tag{1.5}$$

where D_{ref} and D_{ion} are respectively dose of a reference radiation (typically X-rays or gamma rays) and dose of chosen radiation (e.g. protons) that cause same biological effect. It depends on many different parameters such as the biological end point, the particle type and energy as well as the tissue under consideration. According to that, a *quality factor* is assigned to each radiation type to compare, how big biological damage might different type of radiation cause. Multiplying this quality factor with absorbed dose, a *dose equivalent* measured in Sieverts (Sv) could be obtained, which is a normalized measure of the biological effect.

The DNA molecule of the living cells is known as very sensitive target to the incoming radiation that may cause damages like single or double strand breaks or base damages. Typically, this process can happen in two ways:

- *Directly* – the radiation directly hits the DNA molecule causing the disruption of DNA molecular structure.
- *Indirectly* – the radiation interacts with the water molecules inside the cell resulting in free chemical radical production. Since they are characterized by an unpaired electron, they cause structural damage to the DNA mainly by

reacting with its molecule. Moreover, hydrogen peroxide is produced creating a toxic environment for the cell.

For low-LET radiation, the contribution of indirect damage is much higher (about 70%) in comparison with direct DNA damage. On the other hand, for the high-LET radiation the contribution of direct damage is increased [3]. In either case, DNA damage leads to impairment or even loss of a cell function inducing the apoptosis. However, cells are provided with special mechanisms that naturally repair the DNA molecule although, the effectiveness of reparation strongly depends on the damage extent. Nevertheless, the structural changes caused by high-LET radiation are difficult to be repaired leading mainly to the cell death. In particular, the RBE increases with the LET reaching maximum RBE values between 3 and 8 at LET approximately 200 keV/μm and then decreases due to the energy overkill, see Figure 3.

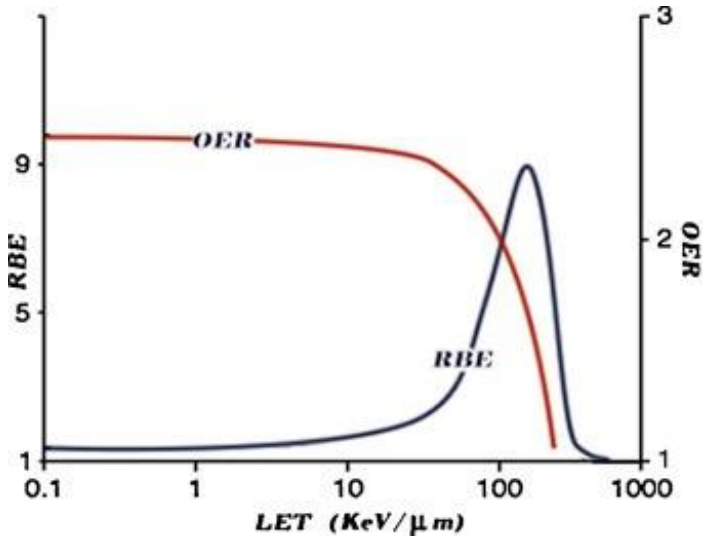

Figure 3: The RBE and OER values as a function of LET [7]

According to [7], it has been found that in majority of cases the cell is damaged via indirect mechanism. Since this mechanism leads to the formation of the reactive oxygen species, the presence of oxygen within a cell has a huge influence on the biological effects of the ionizing radiation. For this reason, the less oxygenated tissues are less sensitive to the incoming radiation. Unfortunately, many tumors are hypoxic or, in case of large tumors, they have hypoxic regions and show significant radio-resistance, especially to the low-LET radiation. To measure such resistance the *oxygen*

enhancement ratio (OER) was established as the ratio of the dose delivered to the hypoxic cell to dose delivered to the well-oxygenated cell to produce same biological effect [3]:

$$RBE = \frac{D_{hypoxic}}{D_{aerobic}} \tag{1.6}$$

In general, the OER decreases as the LET increases and approaches OER of 1 at LET approximately 150 keV/µm, as one can see in Figure 3.

1.2. Radiation cancer treatment

According to the previously mentioned characteristics of heavy charged particles, hadron therapy and, in particular, proton therapy, is one of the most pioneering and well-established methods used for cancer treatment all over the world. However, the conventional radiotherapy that uses high-energetic X-rays beams is still the most widely used for tumor cells destruction [6]. The history of the conventional cancer treatment by X-rays is almost as old as its discovery in 1895.

The X-rays started to be used to treat the malignant tumors just 2 months after its discovery in 1895 by Wilhelm Conrad Röntgen [6]. When such energetic photon beam enters the human tissue it produces Compton electrons that are strongly forwarded scattered and they transport the energy from the surface to the first few centimeters of the body resulting in higher dose delivered to this area, see Figure 4. As it reaches its maximum, the dose drops according to the exponential law by $e^{-\mu x}$, where x is traveled distance of the photon and μ is absorption coefficient of the absorbing medium.

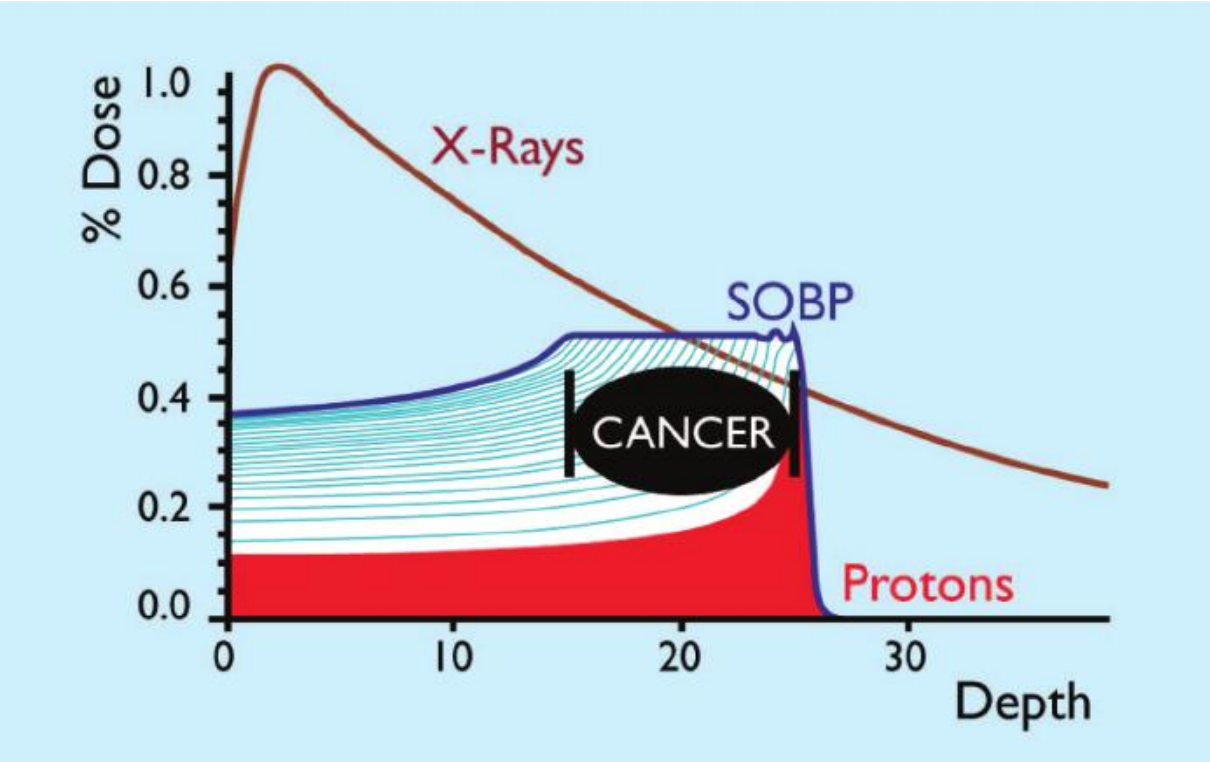

Figure 4: Comparison of the dose delivered to the different depth of the human body for X-rays and protons [8]

For this reason, when treating a deep-seated tumor with a single X-ray beam, the dose delivered to the tumor is generally lower than the one delivered to the healthy tissue situated in front of it. However, using the Intensity Modulated Radiation therapy (IMRT) method, the photon beams are delivered from several different directions (chosen by accurate simulations) lowering the impact of the radiation to the normal surrounding cells. Such high-energetic photon beams are produced by using linear accelerators (LINACs) that accelerate electrons to high energies (up to tens of MeV) which subsequently irradiate the special target producing X-ray radiation.

In comparison with conventional radiotherapy, proton therapy is nowadays used to irradiate the tumor volume with a higher ballistic precision thanks to the Bragg peak formation, as discussed in section 1.1.1. Indeed, due to the Bragg curve most of the dose is deposited at a specific depth in the human tissue depending on the incident proton energy, therefore the tumor can be accurately aimed without causing any significant damage to the surrounding healthy tissue. To deliver the highest dose to the whole

tumor volume, the beam of various proton energies and, as a consequence, penetration depths are superimposed to produce a spread out Bragg peak (SOBP) as shown in Figure 4.

Thanks to the fact that the dose delivered to the normal healthy tissue is significantly lower, the hadron therapy is usually the preferred treatment for the tumors seated next to critical tissues, as for instance nervous system, with respect to the conventional radiotherapy. In particular, hadron therapy and proton therapy have shown to be very efficient to treat brain and ocular tumors, head, neck, lung and prostate cancer. In order to increase the RBE the use of the carbon ions, which dose distribution also follows the Bragg curve, instead of protons has been proposed Due to their higher ionization density at the end of their track, DNA damages occur more often in comparison with protons which increases the RBE (the average RBE for protons is 1.1, while the average RBE of carbon ions is estimated to be 2.5 – 3 [7]). However, carbon ions dose distribution has a tail extending beyond the Bragg peak due to the fragmentation of the ions in primary beam by nuclear interactions. There are few facilities in the world using this Carbon Ion cancer therapy; however, their cost (3 times higher than proton therapy facility [9]) limits their worldwide spread.

1.3 Proton-Boron fusion therapy

Another possible way of increasing the RBE, as proposed [10], in proton therapy is a method based on the proton-boron nuclear reaction. The Proton-Boron fusion reaction has been widely studied for almost 80 years started by Oliphant and Rutherford in early 1930s, [11]. The very first experiments of such nuclear reaction were performed by Cockroft and Walton [12]. In their work they demonstrated that the reaction of an energetic proton beam with boron nuclei ^{11}B might trigger the reaction in which the alpha particles are produced. In the last decades, this reaction has been widely investigated in the energy production field to build an “ultraclean” nuclear-fusion reactor as it produces less than 1% of the energy in neurons [13]. Indeed, such reaction is also called aneutronic fusion.

In particular, the alpha particles can be produced via three main channels:

$$^{11}_{5}\mathrm{B} + p \rightarrow \alpha_0 + ^{8}_{4}\mathrm{Be} + 8.59\ \mathrm{MeV} \rightarrow \alpha_0 + \alpha_{01} + \alpha_{02} \quad (1)$$

$$^{11}_{5}\mathrm{B} + p \rightarrow \alpha_1 + ^{8}_{4}\mathrm{Be}^{*} + 5.65\ \mathrm{MeV} \rightarrow \alpha_1 + \alpha_{11} + \alpha_{12} \quad (2)$$

$$^{11}_{5}\mathrm{B} + p \rightarrow 3\alpha + 8.68\ \mathrm{MeV} \quad (3)$$

When a proton collides with a ^{11}B nucleus the excited ^{12}C* compound nucleus is formed. This nucleus is extremely unstable therefore it decays immediately into an unbound ^{8}Be in its fundamental (1) or excited state (2) while emitting exactly one alpha particle. These particles have a well-defined energy distribution and are referred as α_0 (1) and α_1 (2). In both cases, the ^{8}Be subsequently decays into two secondary alpha particles. The last channel (3) corresponds to the direct 3-body reaction without ^{8}Be formation with released energy of 8.68 MeV in form of kinetic energy given to the alpha particles [13]. Nevertheless, this channel is characterized by significantly low cross section (about 10 μbarn [14]) with respect to channel (1) and (2).

In order to trigger such reaction, assuming the ^{11}B nuclei at rest, the proton needs a sufficiently large energy. According to the theoretical calculations performed in [15], the highest cross-section value of 1.2 about barns was obtained for proton incident kinetic energies between 600 and 700 keV with a resonance at 675 keV [15, 16], see Figure 5. As a result, alpha particles in a wide range of energies from 2.5 up to 5.5 MeV are produced with the dominant energy around 4.3 MeV. Moreover, taking place via channel (2) can generate alpha particles also in higher energy range between 6 to about 10 MeV.

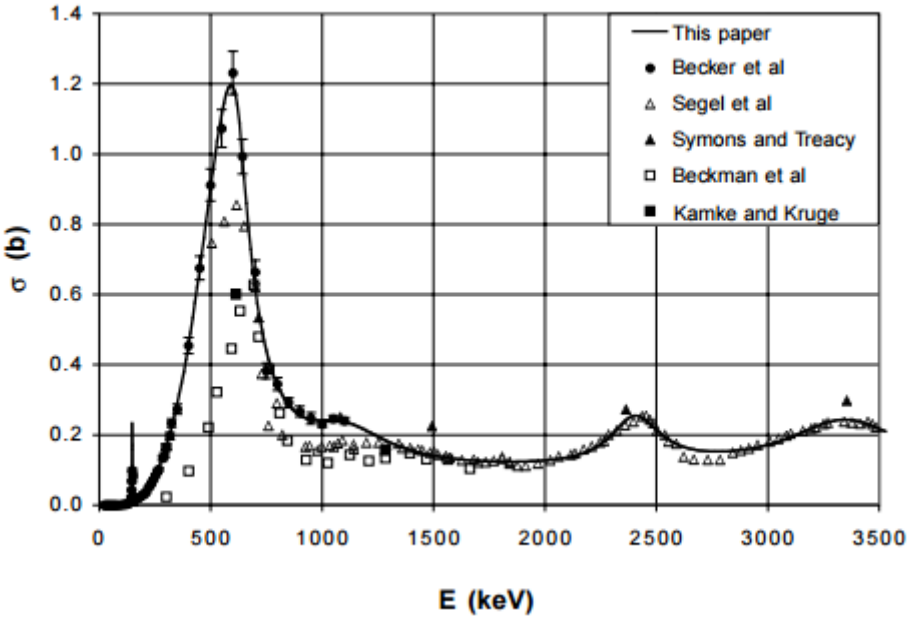

Figure 5: Cross section of the proton-boron reaction as a function of incident proton energy [15]

To take advantage of the Proton-Boron nuclear reaction in proton therapy, the tumor region is injected with a compound labeled with ^{11}B nuclei. The injected region, where the reaction may occur, is usually called the boron uptake region (BUR). The alpha particles produced in the fusion reaction are known as high-LET particles with short range (30 μm) which is comparable with the size of the cell. Therefore, an enhancement in the in delivered dose within the BUR occurs resulting in a more critical damage to the DNA molecules localized in this area. Such proton therapy treatment technique is also known as Proton-Boron Fusion Therapy (PBFT). A pictorial view of the PBFT technique is shown in Figure 6. Since the highest cross section of this reaction has been measured with relatively low proton energies, the number of the reaction events increases as the protons slow down in the area corresponding to the Bragg peak position. For this reason, even higher concentration of ^{11}B present inside the patient body will trigger relatively few or even no nuclear reactions within the proton path to tumor. This effect might lead to an increased effectiveness of the dose localization in comparison with conventional proton therapy. Moreover, the p-B fusion reaction produces 3 alpha particles from each incoming proton, so the high efficiency might be achieved also using lower proton beam intensities.

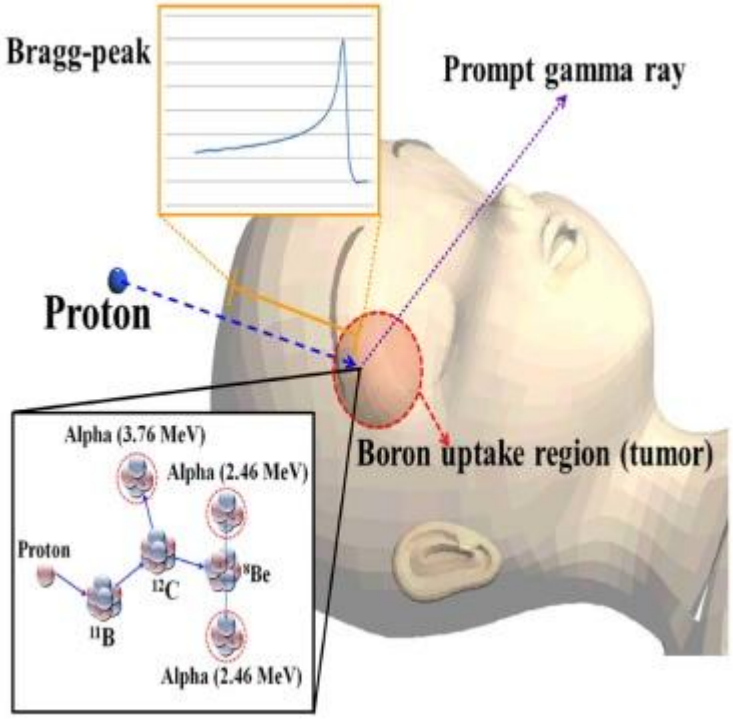

Figure 6: A picturial layout of Proton-Boron fusion therapy [10]

Furthermore, as reported in [10] and shown in Figure 6, this reaction will induce the production of prompt gamma rays of 719 keV from the point where the interaction occurs. Detecting this radiation by gamma camera or single photon emission computed tomography (SPECT) the tumor region could be monitored on-line during the whole therapy.

As it was mentioned before, the machines used for the protons acceleration, namely cyclotrons and synchrotrons, are huge and very expensive which leads to the restriction of their worldwide spread. However, in order to make the proton therapy more affordable for patients, huge effort of researchers has been dedicated to the study of laser-ion acceleration as a more efficient way of high-energetic proton beams production. Next chapter will describe the principle of this widely studied option of acceleration as well as their potential applicability in medical field.

2. Laser-driven ion beams

After the realization of the first laser in 1960 [17], the investigation of light-matter interactions has gathered a lot of interest worldwide. Since then, the advances in laser technology allowed increasing the laser intensities using the Q-switching and mode-locking [19], where continuous wave operation was replaced by the possibility to store laser energy into short laser pulses. Finally, in the last decades, the chirped pulse amplification (CPA), invented by Strickland an Mourou in 1985 [18], allowed to generate laser pulses with maximal achievable intensities up to 10^{22} W/cm^2 [19]. The progress of the laser technology with emphasis on the laser intensity is shown in Figure 7.

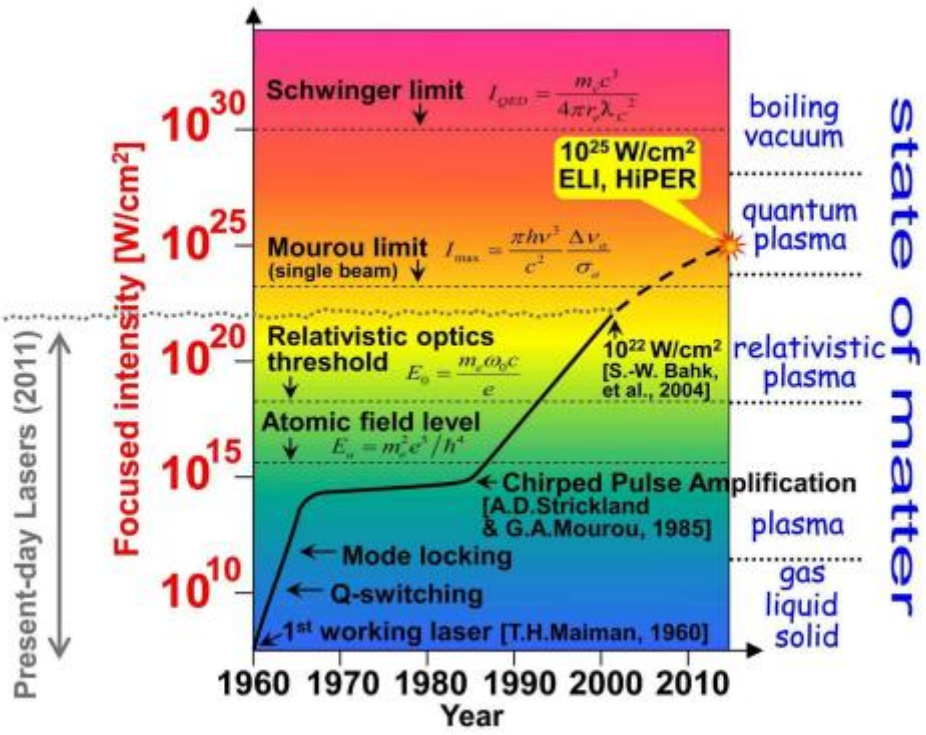

Figure 7: The progress of laser technology starting from 1960 up to new generation of lasers [19]

Currently, conventional particle accelerators, such as linear accelerators, are limited by the breakdown voltage to about 100 MV/m. Moreover, in order to accelerate particles to higher energies (hundreds of MeV), the electric potential has to be applied over the acceleration length from several meters to hundreds of meters. On the other hand, in the laser-driven ion acceleration, the accelerating field present within plasma is not limited by the breakdown voltage that already exceeds several TV/m thus allowing acceleration of particles to MeV energies within a few micrometers.

Laser-driven ion acceleration a is very complex process that involves variety of physical phenomenon at each stage starting from the ionization, the initial plasma formation, the absorption of the pulse energy by electrons, the plasma evolution resulting in ion propagation during and after the acceleration process. When an ultra-high peak power laser pulse interacts with a target, plasma is generated due to the heating and breakdown by a relatively long incoming light.

The first particles accelerated by the laser are the one with the largest charge-to-mass ratio, i.e. electrons. The electron motion is determined by the dimensionless laser amplitude a_0, defined as [21]:

$$a_0 = \frac{eE_0}{m_e c\omega} = \sqrt{\frac{I_0 \left[\frac{\mathrm{W}}{\mathrm{cm}^2}\right] \lambda^2}{\xi_{\mathrm{pol}}\, 1.37 \times 10^{18} \left[\frac{\mathrm{W}}{\mathrm{cm}^2}\,\mu\mathrm{m}^2\right]}} \tag{2.1}$$

where e is electron charge, m_e is electron mass, c is the velocity of light in vacuum and I_0, E_0, ω and λ are the laser peak intensity, the electric field, the angular frequency and the wavelength of the laser light, respectively. The value ξ_{pol} in this equation represents the polarization dependency of I_0, in case of linear polarization $\xi_{\mathrm{pol}} = 1$ and in case of circular polarization $\xi_{\mathrm{pol}} = 2$ [20, 21]. In particular, for the value $a_0 = 1$ the peak intensity I_0 determines the threshold laser intensity to generate the direct laser-ion acceleration to relativistic energies. The threshold for electrons is $\sim 10^{18}\ \mathrm{W/cm^2}$, which turns into $\sim 5 \times 10^{24}\ \mathrm{W/cm^2}$ for protons with $a_0 = 2000$. Therefore, since the maximum laser intensities nowadays obtained are about $10^{22}\ \mathrm{W/cm^2}$, it is not possible to achieve the direct laser ion acceleration.

So far, most of the acceleration mechanisms studied and proposed are based on the generation of the charge separation field. Typically, the electrons are pushed forward by the laser ponderomotive force, defined as the gradient of the time-averaged vector potential [21]:

$$F_{pond} = -\frac{e^2}{4m\omega^2}\nabla\left|\hat{E}(r,t)\right|^2 \tag{2.2}$$

Since the mass m of the ions is much higher than electron mass, the effect of the ponderomotive force on ions is negligible.

During the laser irradiation, a significant number of plasma electrons are accelerated up to the relativistic velocities and for this reason the plasma is called "relativistic plasma". Moreover, under the action of the last part of high-irradiance laser pulse, the motion of the electrons is affected by the presence of electric and magnetic fields following the Lorentz force and the electrons are accelerated towards the laser propagation direction. Since the electrons are pushed forward, they are able to penetrate through the target. On the other hand, heavier ions don't respond to the irradiation as fast as electrons resulting in the formation of a strong electric charge-separation field between the accelerated electrons and the remaining plasma.

Up to now, several acceleration regimes have been theoretically studied, as for instance Target Normal Sheath Acceleration (TNSA) [1], Radiation Pressure Acceleration (RPA) [22] or Break-Out Afterburner (BOA) [23]. Nevertheless, due to the intensity limitation of the lasers available nowadays, the most experimentally investigated acceleration regime, so far, is the TNSA [21].

2.1. Target Normal Sheath Acceleration

TNSA is a mechanism where protons and heavier ions are accelerated from the rear side of the target. Its physical model was firstly described in 1970s [1]. This mechanism has been investigated in most of the experiments performed so far, starting from the early years 2000 using the NOVA Petawatt laser at Lawrence Livermore National Laboratory [1].

The primary interaction of high-intensity short laser pulse with a solid target strongly depends on the contrast of the laser pulse, which is the ratio of the preceding laser light to the main pulse. In TNSA such intensity is exceeding 10^{18} W/cm^2. The interaction of the intense laser pulse with preformed plasma and underlying solid target constitutes a source of electrons with energy spectrum related to the laser intensity. Such so-called hot-electron component has a logarithmic-slope temperature that is roughly equal to the ponderomotive potential of the laser beam, as particle-in-cell calculations have indicated [24]:

$$T_{hot} = \Phi_{pond} = m_e c^2 \left(\sqrt{1 + {a_0}^2} - 1\right) \tag{2.3}$$

The conversion efficiency from laser pulse to hot-electron cloud is regulated by the following expression and the total number of electrons n_0 is calculated as [24]:

$$n_0 = \frac{\eta E_L}{c\tau_L \pi {r_0}^2 k_B T_{hot}} \tag{2.4}$$

where η is a fraction of laser energy converted to hot electrons, E_L and τ_L are laser pulse energy and duration, respectively, c is the speed of light, k_B is Boltzmann constant T_{hot} electron plasma temperature and r_0 is laser spot radius. The η scales with laser intensity Ias [24]

$$\eta = 1.2 \times 10^{-15} I^{0.74} \tag{2.5}$$

Since modern laser systems are able to deliver ultra-short (less than picosecond) high-intensity laser pulses, plentiful amount of energetic electrons are generated in comparison with the electrons in the plasma generated by longer laser pulse. These electrons have typical energies in the MeV range, so their mean free path is much longer than the target thicknesses usually used in experiments (targets are usually few μm thick while the mean free path of electrons with temperature 1 MeV is around 0.4 mm [25]). When the electrons propagate through the target, constituted current exceeds the Alfvén limit by several orders of magnitude, as explained in [24]. For this reason, in order to minimize generated magnetic field, such current must be compensated by

return currents. The return currents will be driven by the charge separation that occurs during laser-plasma interaction and strongly depends on the electrical conductivity of the target. Without return currents, the electron would be stopped within a distance less than 1 nm [24].

When the electrons reach the rear side of the target, they form a dense charge-separation sheath creating an electric field. This electric field is strong enough to deflect electrons back into target resulting in a continuous electron recirculation. This charge-separation field ionizes the atoms of the target and, then, the created ions start to expand into the vacuum, following the electrons. Schematic depiction of the TNSA regime is shown in Figure 8.

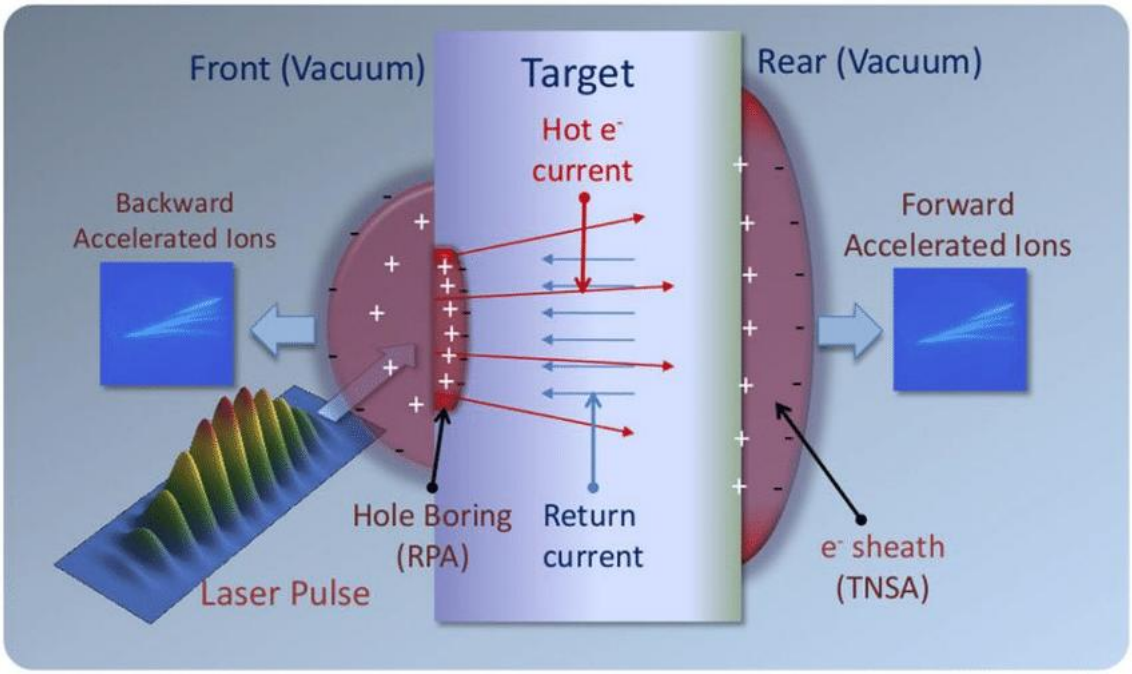

Figure 8: A pictorial view of the TNSA regime. **[**26]

Simple physical models based on plasma expansion in vacuum have been developed to describe this particular type of ion acceleration and are discussed in [20]. In this work, the authors assume that the ions of the target are initially at rest and form a boundary with the vacuum. On the other hand, electrons exhibit a Boltzmann distribution with the electrostatic potential Φ [20]:

$$n_{hot} = n_0 \exp\left(-\frac{e\Phi}{k_B T_{hot}}\right) \tag{2.6}$$

The electrostatic potential follows the Poisson equation [20]:

$$\frac{\mathrm{d}^2\Phi}{\mathrm{d}x^2} = 4\pi e(n_{hot} - Z_i n_i) \tag{2.7}$$

In equation (2.6) and (2.7) n_{hot} determines the density of hot electrons, Z_i and n_i are respectively ion charge and density. As one can see in equation (2.7), the models are one-dimensional. As plasma expands, significant charge separation occurs over a distance known as Debye length [24]:

$$\lambda_D = \sqrt{\frac{\varepsilon_0 k_B T_{hot}}{n_{hot} e^2}} \tag{2.8}$$

The initial electric field is given as [24]:

$$E_{sheath,0} = \sqrt{\frac{2}{e_N}}\frac{T_{hot}}{e\lambda_D} = \sqrt{\left(\frac{8\pi}{e_N} n_{hot} T_{hot}\right)} \tag{2.9}$$

The e_N in this equation represents the Euler number. The lines of the electric field are parallel to the normal vector of the target rear side, so the acceleration follows mainly this direction. This field remains as long as the electron temperature is high, or as long as the laser pulse keeps accelerating electrons at the target front side. The most likely ion species to be accelerated are protons, as they have the highest charge-to-mass ratio. They leave the target with hot electrons forming a quasi-neutral plasma cloud. As protons expand, their positive charge causes a decrease of the peak electric field as it becomes partly shielded. For this reason, the acceleration becomes less efficient in case of long duration laser pulses. However, for short laser pulses, the acceleration time is given by the pulse duration and not by the ion expansion. One can say that the acceleration lasts as long as the laser pulse is present.

In principle, particles can be accelerated from both sides of the target since the energetic electrons initially accelerated in the laser are reflected even at the front side of the target

due to the space-charged fields. As the electrons are able to circulate between both surfaces, they lose their energy and spread out which results in the heating up the target volume. According to TNSA model, the pre-pulse generates plasma at the front side of the target with longer scale lengths, which according to equation (2.9) results into generation of much lower electric fields and which subsequently leads to the production of particles with significantly lower energies than particles in forward direction.

2.1.1. Maximum proton energies

As reported in [27], the determination of maximum ion energies E_i is accelerated from the rear side of the target is still questionable and it depends on the electron temperature T_{hot} as follow:

$$E_i = \alpha T_{hot} \tag{2.10}$$

In this equation α represents coefficient that is changing according to different experimental conditions. Recently it was found that the maximum energy depends on the target thickness as well. The electron recirculation within the generated electric field enhances the sheath acceleration. Since the velocity of the hot electrons is approximately the velocity of light *c*, one can say that the hot electron bunch length is the same as the laser pulse length L_p. The electrons travel through high conductive target without any energy loss and then they are reflected at the target surface by itself induced sheath field. If the target thickness L is greater than half of the pulse length $L_p/2$, the electrons overlap only locally at the target edge without any significant increase in hot-electron density. However, when the target is thinner than $L_p/2$, the recirculating electrons increase the electron density with dependence on the target thickness. According to the [27], the recirculation process does not increase the temperature of hot electrons, which remains almost the same. It is expected that when proton passes through the potential created by the hot-electron shield, it will gain the same energy as the maximum electron energy E_{eMAX}. The simulations, performed in [27], proposed the empirical scaling of the maximum ion energy depending on the target thickness L:

$$E_i = \left(\frac{L_c}{L}\right) E_c \approx \left(\frac{L_c}{L}\right) E_{eMAX} \tag{2.11}$$

In this case, L_c denotes the critical distance, which is equal to $L_p/2$ and it represents a thickness of the target in which the circulation time is longer and the acceleration occurs raggedly. Nevertheless, this approximation is highly idealized since in reality the electrons are losing their energy during the recirculation, especially at the edge of the target, where ions are accelerated. Moreover, when considering the multidimensional situation, the hot electrons angular spread reduces the recirculation effect.

However, according to the expansion of proton distribution, as mentioned above, the shielding effect of their positive charge must be taken into account. As shown in [1], an analytical expression describing the evolution of maximum proton energy E_{pMAX} as a function of pulse duration τ_L can be written as follow [1]:

$$E_{pMAX} \approx 2k_B T_{hot} \left[\ln\left(\frac{\omega_p \tau_L}{\sqrt{2e_N}} + \sqrt{1 + \frac{{\omega_p}^2 {\tau_L}^2}{2e_N}} \right) \right]^2 \tag{2.12}$$

where ω_p is the proton plasma frequency. Here, the maximum energy of protons accelerated from the rear side of the target ϵ_{pMAX} depends only on the pulse duration, the temperature of hot electrons and the initial hot electron density n_{e0} at the rear side, since $\omega_p = \sqrt{n_{e0} e^2/\varepsilon_0 m_p}$. The proton energy spectrum predicted by the self-similar solution is expressed as [1]:

$$\frac{\mathrm{d}N_p}{\mathrm{d}E_p} = \frac{n_{i0}}{\sqrt{m_p E_p}} \exp\left(-\sqrt{\frac{2E_p}{k_B T_{hot}}} \right) \tag{2.13}$$

This energy spectrum would extend to infinite proton energies and the number would be increased for longer interaction times. However, the protons show energy cut-off due to the formation of a proton front during the acceleration process. For this reason, the energy spectrum would extend up to the peak energy given by the protons situated at the front side of the target.

2.1.2. TNSA beam parameters

The TNSA regime is the most widely theoretically and experimentally investigated mechanism in literature [1, 21, 26, 28]. Protons are the lightest ions and have the highest charge-to-mass ratio therefore they are more likely to be accelerated. These protons are present in the target either as contaminants of the surface (from water vapor and hydrocarbon contamination) or as compounds of the target. The cloud of accelerated protons from the target surface shield the electrostatic field created by the hot electrons for other ion species, therefore for successful heavy ion acceleration the protons and light ions contaminants removal is necessary. Since the particles are accelerated from different target depths, they reach different maximal energies which leads to the generation of wide range energy spectrum with a cut-off energy given by the driving electron temperature. The number of protons accelerated per shot is typically of the order of 10^{13} [24]. The opening angle of the protons increases as the proton energy decreases, see Figure 9. Protons with the highest energy are most likely accelerated in the target normal direction with an angular cone less than 5° half angle [24]. Typically, laser-driven ion beams show wide angular aperture that can vary from 30° to 40° half angle.

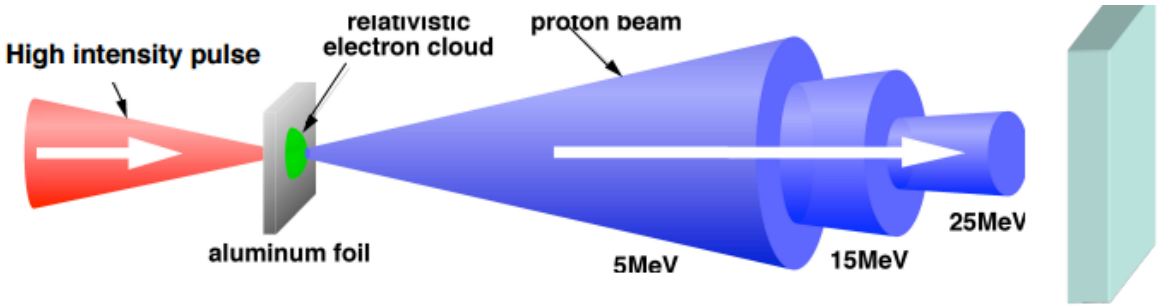

Figure 9: Increasing opening angle with decreasing proton energy [29]

Summarizing, laser-driven ion acceleration has a huge potential in different multidisciplinary fields as it produces multi MeV ion beams with extremely intense fluxes order of magnitude more intense than conventional acceleration. Moreover, very high acceleration gradients can be achieved in a very short distance and their values are orders of magnitudes superior to conventional radio-frequency sources. Therefore, the

beam delivery is very compact in a much smaller footprint and with lower corresponding facility costs [30]. Nevertheless, in comparison with conventionally accelerated proton beams, laser-target interaction shows low shot-to-shot reproducibility.

The characteristics of such beam depend predominantly on the laser and on target parameters, such as target thickness and material. A low-Z material target is preferable, since the electrons can distribute the part of the energy provided by the laser into bremsstrahlung for higher-Z materials. The thickness of the target is determined by the laser contrast because TNSA requires a sharp density gradient at the rear surface.

Rising the laser intensity can, in principle, lead to increasing the particles energy. For this purpose, new generations of laser facility are under construction to deliver a laser beam with intensity exceeding the current achievable limit. One particular is under construction in Czech Republic and will be described more in details in next chapter.

2.2. ELI-Beamlines facility

ELI-Beamlines facility is one of the three pillars of Extreme Light Infrastructure (ELI) responsible for the development of ultra-short pulses of high-energy particles and radiation originating from relativistic and ultra-relativistic interactions. Such laser system will deliver laser pulses with high repetition rate ($1 - 10$ Hz), ultra-high peak power (10 PW) and focused intensities up to 10^{24} W/cm^2 [31]. The main aim of the Eli-Beamlines facility is to become a multidisciplinary and user oriented infrastructure for performing scientific experiments and applications in different fields, including the medical one, by combination of advanced synchronized short laser pulses with secondary sources of particles and radiation. Eli-Beamlines facility will provide a variety of secondary sources, mainly based on entirely new concepts, driven by ultra-intense lasers allowing the production of radiation and particles pulses with very high intensity and quality over a broad spectral range.

This facility will provide laser pulses from four different laser systems. One of them, namely L3, will supply the experimental hall E4 where the user-oriented ELIMAIA

(ELI Multidisciplinary Applications of laser-ion Acceleration) beamline will be installed within 2017. The technical layout of the beamline is shown in Figure 10. This beamline will allow users to test various sample with the ion sources accelerated by interaction of 1 PW laser pulse, with energy up to 30 J and pulse duration of 30 fs, with a solid target at high repetition rate (1 – 10 Hz) [2]. In addition, in a second phase 10 PW long-pulse laser with energy of 150 J, pulse duration of 150 fs and repetition rate of 1 shot/min will be available for the laser-acceleration experiments [2]. Furthermore, the investigation of innovative schemes for laser-driven ion acceleration will be possible within the flexible interaction chamber.

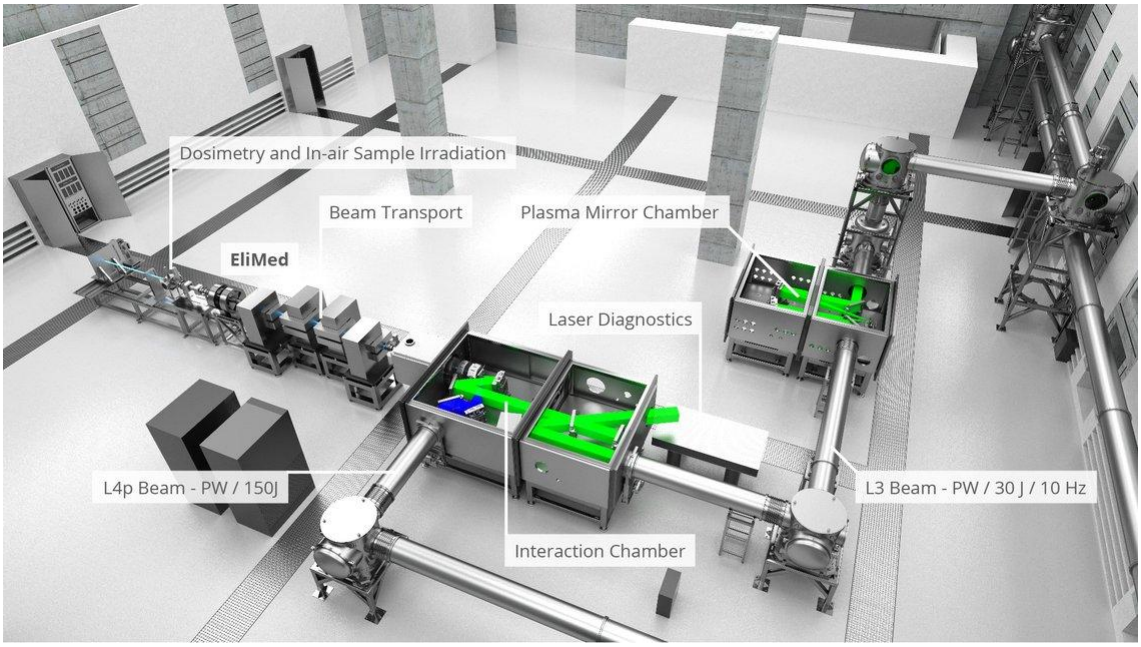

Figure 10: Technical layout of the experimental hall E4 with all components of the ELIMAIA beamline [31]

2.3. ELIMAIA beamline

The ELIMAIA user beamline, see Figure 10, consists of two main sections. The first one is dedicated to transport the laser pulse to the target and to the ion acceleration composed of a plasma mirror chamber (PM) and a target interaction chamber (TC). The second section, named ELIMED (ELI-Beamlines MEDical and multidisciplinary applications), is dedicated to transport, selection, diagnostics and dosimetry of laser-driven ion beams and it has been developed and realized by INFN-LNS (National

Institute for Nuclear Physics – Laboratori Nazionali del Sud, Catania, Italy) in collaboration with ELI-Beamlines. The main aim of the beamline is to deliver to the users stable and reproducible ion beams with spatial homogeneity, fluence and energy spread very similar to the conventionally accelerated beams [2].

The ELIMED beamline section is divided into two main parts: vacuum and in air sections. The vacuum part will be dedicated to transport, selection and diagnostics of optically accelerated ion beams. This section begins with a permanent magnet quadrupole system (PMQs) placed few cm downstream the target to collect and focus particles of interest. Subsequently, the beam enters an energy selector system (ESS) which allows selecting particles in terms of energy and species. The ESS is a set of four resistive magnetic dipoles that operates as a magnetic chicane on a fixed reference trajectory. Such system allows the selection of protons with energies up to about 300 MeV and carbon ions up to 70 MeV/n [2, 32], with the energy resolution given by central slit aperture ranging from 5% to 20% according to the slit aperture and the transmission efficiency achievable [2]. The final - in air section - provides relative and absolute dose measurement of the ion beam delivered to the irradiation point. The schematic layout of the beamline with all the components is shown in Figure 11.

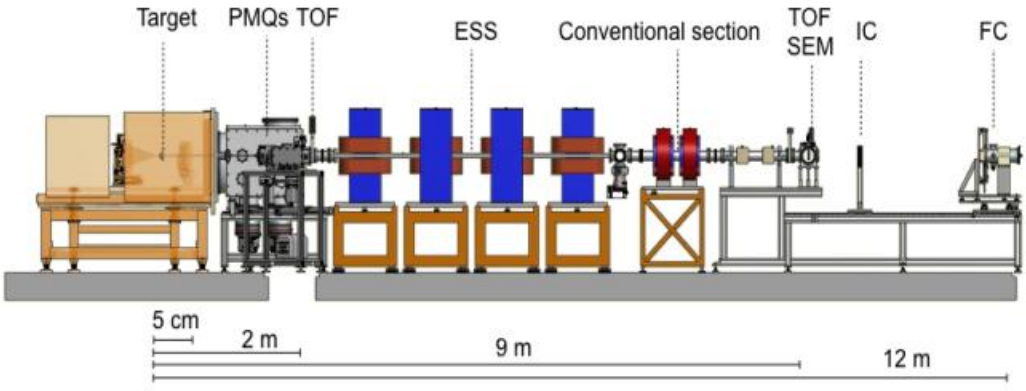

Figure 11: Technical layout of the ELIMED beamline with all components at given distances [33]

Due to the extremely high dose-rate of the laser-driven ion beams it is not possible to use conventional dosimetric systems as well as dose-rate dependent dosimetric devices.

According to these limitations, a specially designed Faraday Cup (FC) will be used for absolute dosimetry at the end of the beamline together with the multi-gap ionization chamber (IC) for the relative dosimetry. FC is able to collect the charge without dose-rate dependency and the IC is characterized by high charge collection efficiency. A secondary emission monitor (SEM) will be used as on-line detector providing information on the beam current [33].

2.4. Diagnostics system for ELIMAIA beamline

The laser-driven ion beams exhibit extreme characteristics different from the conventionally accelerated ones. Such high peak current (10^{12} p/bunch), short pulse duration (0.1 – 1) and high dose-rate in a single pulse (10^{9} Gy/min) do not allow us to measure the beam characteristics using the traditional particle detectors [2]. For this reason, innovative techniques for particles detection have to be developed in order to ensure delivering a beam suitable for multidisciplinary applications. The main diagnostics system developed for the ELIMAIA beamline is based on the time-of-flight (TOF) method. The TOF is one of the most established methods used in laser-driven ion acceleration exploited so far in several low intensity and low repetition rate laser system experiments [2, 34, 35].

The detector for laser-driven ion beam diagnostics has to fulfill several requirements, such as radiation hardness, due to the huge number of particles accelerated by the laser-target interaction (several orders of magnitude higher than the conventional one), and high signal-to-noise ratio, due to the electromagnetic pulse present in such environment. Moreover, since the detectors will be used in TOF configuration, the fast charge collection and the low capacitance are crucial requirements in order to measure with good time resolution allowing to determine maximum cut-off energy of the fastest ions and possibly to discriminate different components of the incoming beam.

In fact, however never used at such high ion energies, the TOF technique is one of the most established diagnostics method mainly used in low-energy laser-driven beam experiments and low repetition rate laser system, e.g. through the use of Faraday cups (FC) or Ion collectors (IC). Nevertheless, the low time and energy resolution of these

detectors limit the time separation of the different accelerated species and charge states, required for the identification and energy reconstruction, particularly, for high energy ion beams. For these reasons, SiC and diamond detectors, according to their advantageous properties, are the most appropriate for the high energy proton beam diagnostics [2, 33].

This measurement could be acquired by using detectors like Faraday Cups or ion collectors. However, according to their low time and energy resolution, the separation of different accelerated species with different charge state is limited especially when detecting high-energy particles. Moreover, considering high repetition rate delivered at ELIMAIA, these detectors are not able to provide on-line shot-to-shot information about the beams parameters, which is crucial for monitoring and controlling beam delivered for different kind of applications. For these reasons, the silicon carbide (SiC) and diamond detectors have been chosen as the most suitable detectors according to their advantageous properties [33].

These detectors will be mounted along the ELIMAIA beamline at two different distances from the target. First detector will be placed at approximately 2 m downstream the target to monitor stability and reproducibility of the beam parameters after focusing system. Second one will be mounted at about 9 m downstream the target at the end of the vacuum beamline section. At this stage, the beam will be monitored in terms of maximum energy cutoff bandwidth and fluence coming out of the selection system. Both TOF detectors will provide information that allow optimizing the transport and adjusting the PMQs and ESS parameters according to the required beam specification [2].

2.5. Time of flight detectors

Diamond and SiC detectors, chosen as the most appropriate diagnostic devices for laser driven ion beams, can be described as solid-state semiconductor detectors due to their similar operational characteristics. Semiconductors are crystalline materials whose outer shell atomic levels exhibit an energy band structure. The lower band, the valence band, is composed of electrons bounded to specific sites inside the crystal. On the other hand, the upper band, called conduction band, contains free electrons that contribute to the

material electrical conductivity. These two bands are separated by the forbidden band or *bandgap*. The width of this band determines the conductivity classification of the material – whether the material is conductor, semiconductor or insulator – as one can see in Figure 12.

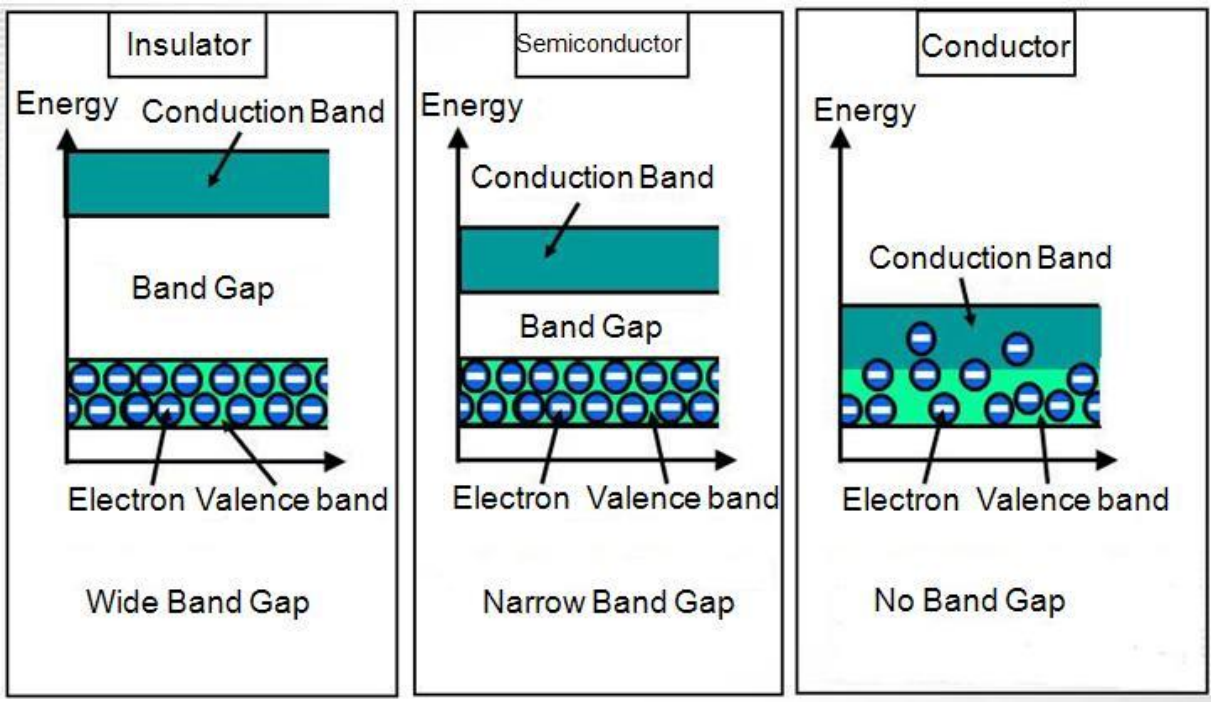

Figure 12: Classification of the materials to the group of conductors, semiconductors or insulators according to the bandgap energy [36]

The detection process is based on the electron-hole generation inside the detector in case of radiation with energy in excess of *bandgap* energy passes through the material. The energy deposition due to the energy loss of the particle leads to the creation of equal number of electrons and holes along its track. The average energy necessary to create an electron-hole pair is known as ionization energy ε and it depends on the detector's material. Generated charge carriers are then tent to move simultaneously and recombine very quickly. However, if an electric field is applied to the detector, the charge carriers are drifted toward the detector electrodes in opposite direction. The drift velocity of electrons and holes depends on their mobility and on the external voltage applied as follow [4]:

$$v_e = \mu_e E \tag{2.14}$$

$$v_h = \mu_h E$$

where μ_e and μ_h are the mobilities of the electrons and holes respectively and E is the magnitude of the electric field.

Their motion results in a current pulse that persists until the free charges are collected by the electrodes. The amplitude of the output voltage is directly proportional to the radiation energy loss in the active volume, therefore, to the number of electron-hole pairs generated and collected.

Semiconductors may operate either as an intrinsic semiconductor (in case of diamond detector) or as a junction (in case of SiC detector). A junction is created when two different types of semiconductors (p-type and n-type) are brought together into good thermodynamic contact. Since the concentration of the charge carriers inside those two materials is different, there is an initial diffusion of holes towards p-region and electrons towards n-region. As a consequence, their recombination causes a charge build-up to occur on both sides of the junction. This creates an electrical field gradient across the junction and the region of changing potential is known as the *depletion zone*. In principle, any electron-hole pair created within this region is swept out by the electric field making this region suitable for radiation detection. In addition, if a reverse-bias voltage is applied to the detector, it will attract the holes in the p-region away from the junction as well as electrons in the n-region enlarging the depletion zone. Moreover, the higher external voltage will also provide a more efficient charge collection. However, maximum applied voltage is limited by the resistance of the semiconductor because at some point, the junction will break down and begin to conduct [4, 5].

The physical and electrical properties of SiC and diamond detector are listed in Table 1. Semiconductor detectors provide excellent performances thanks to their high speed of response and high efficiency. Moreover, they are able to reach high energy resolution even at room temperatures.

Table 1: Table of the SiC and diamond detector properties [37]

	4H-SiC	Diamond
Relative dielectric constant	10	5.5
Bandgap energy(eV)	3.26	5.45
Electron mobility (cm^2/Vs)	1000	2200
Hole mobility (cm^2/Vs)	50	1600
Thermal conductivity (W/cmK)	4.9	22
Electron-hole pair generation energy (eV)	7.8	13
Threshold displacement energy (eV)	21 – 35	40 – 50

2.5.1. Silicon Carbide detector

The development SiC detectors have raised large interest in the detection of ionizing radiation, especially X-ray, protons, alpha particles and ions [38]. The wide bandgap energy and low concentration of intrinsic carriers allow SiC to operate at much higher temperature than silicon. Moreover, it provides only negligible leakage current which leads to low noise level. The SiC material might exist in many different polytypes. These polytypes are composed of different stacking sequences of Si-C bi-layers which simplistically are planar sheets of carbon coupled with planar sheets of silicon atoms. The most common polytypes are 3C-SiC, 4H-SiC and 6H-SiC, where the number in the acronym stands for the number of bi-layers and ‘H’ and ‘C’ for hexagonal and cubic, respectively. The different stacking of the bi-layers affects the electronic and optical properties of the material, e.g. the bandgap energy. For the radiation detector realization, 4H-SiC polytype is preferred, [38].

The construction of SiC detectors for radiation detector application is realized by two doped 4H-SiC epitaxial layers and by one rectifying Schottky junction above the active region. Moreover, the ohmic contact to the highly doped SiC is provided in order to ensure the ideal electrical current carrying without parasitic resistance. In such composition, the Schottky contact, usually realized by different metals (Ni or Au)

serves as anode as it collects generated electrons while bottom highly doped SiC layer works as cathode. The schematic layout of the detector is shown in Figure 13**.**

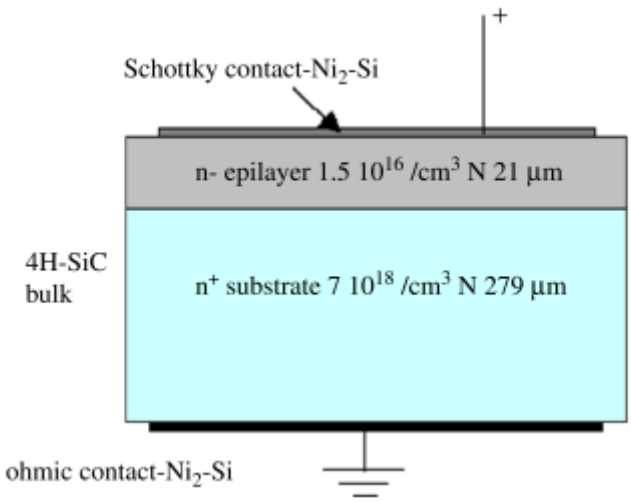

Figure 13: The schematic layout of the 4H-SiC detector [39]

Thanks to the wide bandgap of approximately 3.2 eV, the detector provides only negligible leakage current that leads to low noise level even at high temperature. Moreover, it can operate under the exposure of the visible light because optical photons have insufficient energy to produce electron-hole pairs. With high saturation velocity of the charge carriers ($2 \cdot 10^7$ cm/s) and the high breakdown field (2 MV/cm) the response of the detector is extremely fast and less sensitive to the charge trapping [38].

2.5.2. Diamond detector

Diamond is one of the allotropic forms of carbon with stable structure in which every atom has four covalent bonds constituting a regular tetrahedron. According to the rigidity of the diamond lattice, it is considered as the hardest known substance. Its extreme stability defines its physical properties in many ways, e.g. the melting point is the highest of any known material (4363 K) [40]. The electrical properties are strongly determined by its bandgap (5.45 eV). This energy is much higher than typical thermal energies, therefore at room temperature with the high material resistance ($10^{11} - 10^{16} \Omega$cm) in electrical terms it is consider to be an excellent insulator. However,

diamond is often referred to be as a semiconductor according to its similarities with the conventional semiconductors such as germanium or silicon.

Just like SiC detectors, the properties of the diamond detectors mentioned in Table 1 determine them to be a great alternative to silicon semiconductor detectors in the detection of high-energy ions, charged particles and photon radiation. The artificial diamonds typically used to realize diamond detectors are produced using a Chemical Vapor Deposition (CVD) process. During this process, a thin layer of the material is built up by its deposition on the suitable substrate from a gas phase, which typically contains hydrocarbon gases and hydrogen operating at low pressure. This technology allows the low-cost production of diamond with purity higher than the natural one.

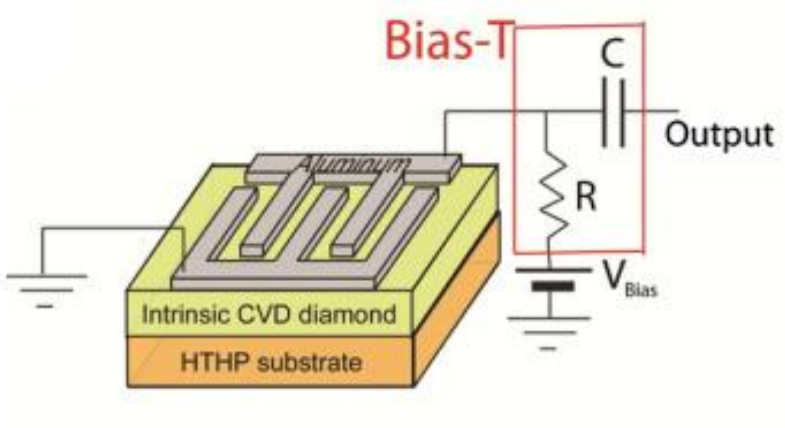

Figure 14: The schematic layout of the diamond detector [41]

In the Figure 14, one can see the schematic layout of a diamond detector. In this case, the intrinsic diamond layer was deposited by CVD technique on the commercial synthetic High Pressure High Temperature (HTHP) diamond substrate. The intrinsic layer represents the sensitive detecting region of the detector. On the top of this layer the aluminium electrodes were patterned by thermal evaporation in the standard lift-off photo-lithographic technique. If an external voltage is applied between the electrodes, an electric field perpendicular to the incoming radiation is generated [41]. The interesting characteristics of diamond, such as high-thermal conductivity, high resistivity, low dielectric constant, high carrier mobility and radiation hardness, suggest that this material is ideal for monitoring of radiation emission from laser-generated plasmas [41]. Moreover, thanks to its fast response time, these detectors could be employed in the TOF measurement for detection of protons and heavy ions.

3. Methods

The experiment “Laser induced aneutroic fusion reaction by advanced materials” has been performed at Prague Asterix Laser System (PALS) laboratory in November 2017. The main aim of this experiment was to maximize the number of alpha particles produced in the proton-boron fusion using specially prepared thin targets and relatively long laser pulse (sub-nanosecond). The targets, during the experiment were doped with hydrogen and boron atoms. In this experiment, different radiation detectors were mounted within the interaction chamber to measure the angular distribution of the alpha particles emitted from the target surface, namely SiC and diamond detectors in TOF configuration, CR-39 tracking detectors and Thompson parabola spectrometers. The experimental setup mounted during the experiment is shown in Figure 15. The target was tilted by 30° with respect to the incoming laser beam.

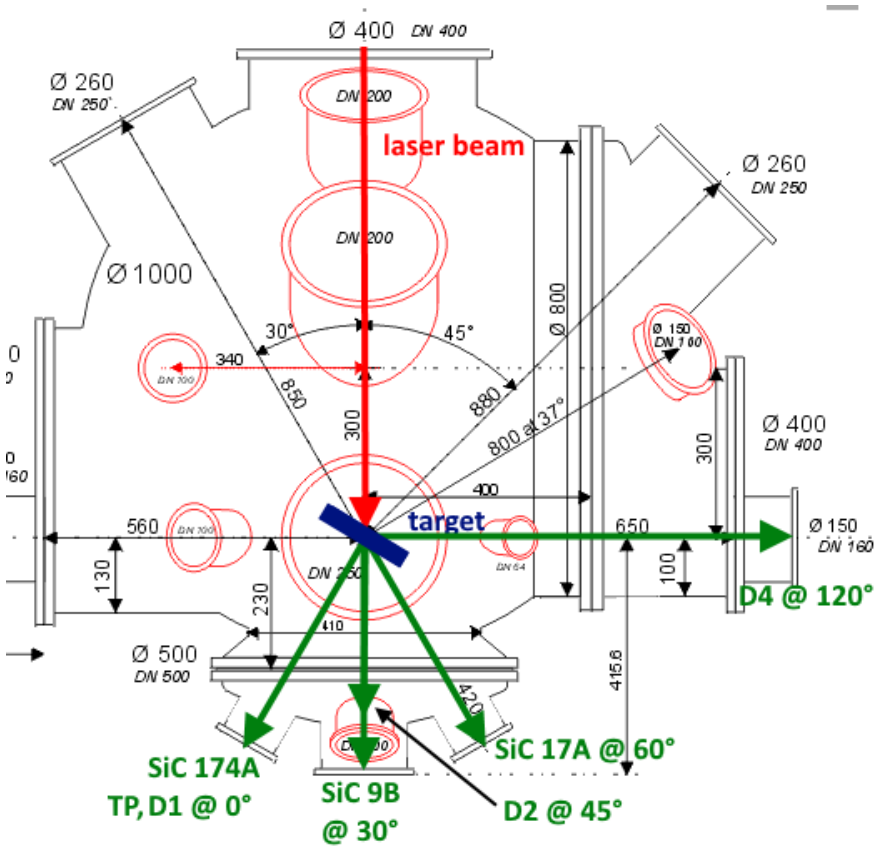

Figure 15: Experimental setup at PALS interaction chamber indicating the position of all TOF detectors as well as Thompson parabolas.

3.1. Prague Asterix Laser System (PALS)

The experiment has been performed using the high-power iodine laser system named Asterix IV. The Asterix IV laser operates at the fundamental wavelength 1315 nm and is able to deliver laser pulses with a 1 kJ nominal energy with usual maximal energy delivered to the main interaction chamber at about 600 J [42]. The time duration of the laser pulse is about 350 ps with a peak power of 3 TW (for the beam of energy 600 J delivered into the chamber is approximately 2 TW). The laser is able to fire full-energy shot every 25 minutes with the power density on the target up to 3×10^{16} W/cm^2[42]. The laser pulse delivered at PALS exhibits spatial profile quality and high shot-to-shot stability.

The laser beam is generated in the first part of the laser system – oscillator. Initial laser pulse is then traveling along the chain of five amplifiers with sequentially increasing size. Such an arrangement is called Master Oscillator Power Amplifier (MOPA). The amplifiers are cuvettes filled with perfluoroisopropyl iodide C_3F_7I gas. This laser system uses neutral iodine atoms in order to produce near-infrared light at the wavelength of 1315 nm. The laser beam of such wavelength is produced by releasing the iodine atoms from the C_3F_7I molecule in a photochemical process called photo-dissociation. This reaction is caused by UV radiation created by flashlamps surrounding the amplifier cuvettes. The iodine atom released is in its excited state providing the inversion of population thereby constituting the conditions for lasing action. [42] As the laser beam travels along the chain, its diameter is increasing (from the initial 3 mm at the output of the oscillator to the final 290 mm at the output of the amplifier section) thanks to the spatial filters placed between the amplifiers. These filters are telescope-like devices and consist of two convex lenses with common focus [42]. Last part of the PALS laser system that will be mentioned is Faraday rotator. This device is placed 3rd amplifier and 4th spatial filter in order to prevent from damaging of the first part of amplification system caused by back-reflected beam. The schematic layout of the whole laser system is shown in Figure 16**.**

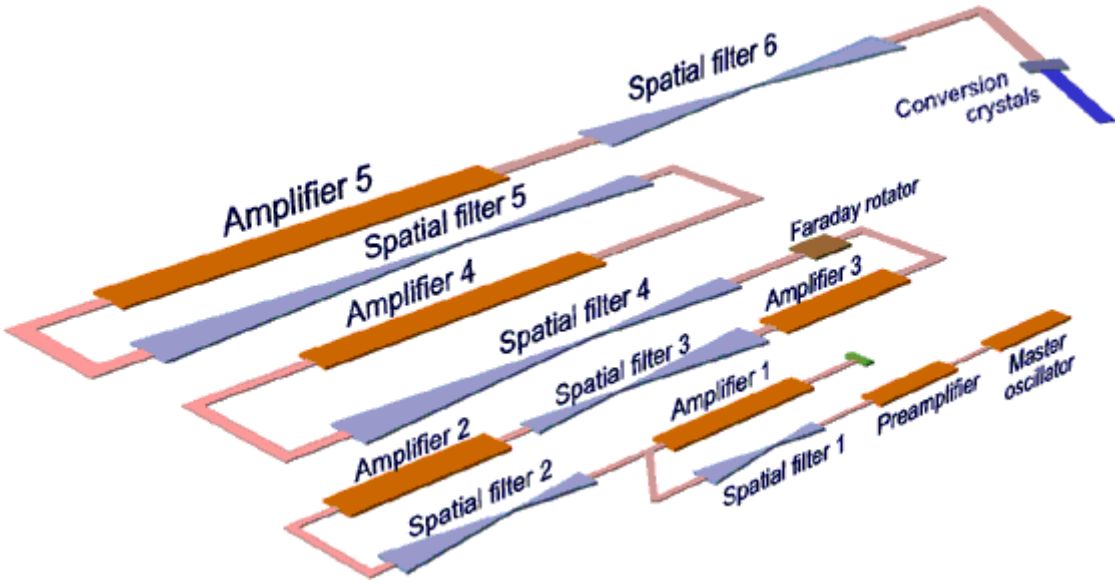

Figure 16: The schematic layout of the laser system at PALS [42]

Besides the main beam, the Asterix IV system delivers an auxiliary beam that is obtained by splitting-of fraction of the 4th amplifier using a semi-transparent mirror. The main outcoming parameters of the Asterix IV at PALS are listed below in Table 2. [42]

Table 2: Parameters of the main and auxiliary beam delivered at PALS [42]

General	Fundamental wavelength	1315 nm
	Pulse duration	200 to 350 ps
	Pulse contrast (prepulses & ASE)	$\sim 10^{-7}$
	Repetition shot rate	25 min
	Output energy stability (over 10 shots)	$< \pm 1.5$ %
Main beam	Pulse energy at 350 ps	1 kJ
	Pulse power at 350 ps	3 TW
	Diameter	290 mm
	Conversion efficiency to 3ω	55 %
Auxiliary beam	Pulse energy at 350 ps	100 J
	Diameter	148 mm
	Conversion efficiency to 3ω	30 %

The laser-target interaction area is provided with two vacuum chambers – the master target chamber and the second target chamber, see Figure 17. Both beams, main and auxiliary, could be delivered to the both chambers. The internal optics and the target holder are mounted on a support frame directly attached to the floor, mechanically separated from the chamber walls and balanced in order to ensure the position stability of the target. This system prevents the relative motion of the mounted components due to the flexing of the chamber walls during the pump down. [42]

Figure 17: Master (on the left) and secondary (on the right) interaction chamber at PALS [42]

For the experiment, for the object of this thesis the setup was mounted on the master target chamber, see Figure 17. This chamber is composed of a vacuum spherical section made of stainless steel with the diameter of 100 cm, equipped with a hinged elliptic cap with diameter of 80 cm that serves as an entrance port. For the diagnostics and alignment purposes, the chamber is equipped with 15 circular ports with diameter ranging from 64 mm to 500 mm.

3.2. Targets

The targets we used were specifically fabricated for this experiment at the Micro-Nano Facility of Fondazione Bruno Kesler in Trento, Italy. The doping procedure is based on

thermal annealing and ion implantation processes allowing the development of specific targets for triggering the proton-boron fusion reaction by controlling the concentration and implantation depth of the doped elements.

Three different thin targets were used: 6.5 μm thin solid Aluminium foil as a reference target and two different 10 μm Si targets doped with hydrogen and boron layers. In particular, the 10 μm thick Silicon layer was doped by boron atoms in a depth of 200 nm in the matrix forming a layer with the thickness of 100 nm and boron concentration of 1×10^{22} cm^{-3}. The concentration of hydrogen atoms was increased by thermal annealing in which hydrogen atoms diffuse into Si matrix where they form Si-H bonds reaching the concentration of 5×10^{22} cm^{-3}. A 5 μm photoresist PR layer (CH compound) with density of 1 g/cm^3 was added to one of the SiH-B target type surface. The structures of the doped SiH-B targets with and without the PR layer targets are shown in Figure 18 a) and b) respectively.

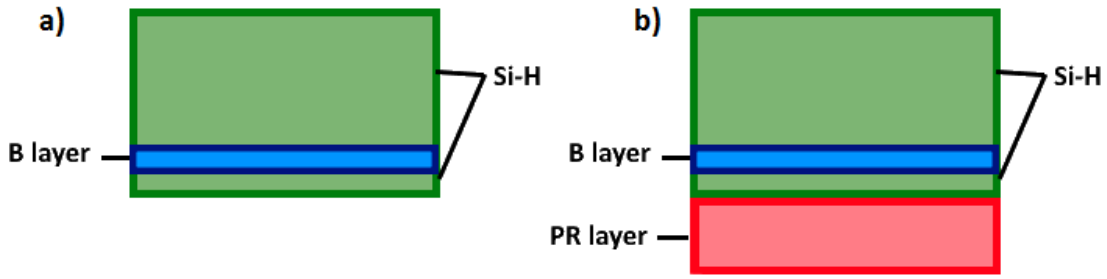

Figure 18: Schematic layout of the target layers: a) SiH-B target and b) SiH-B target with photoresist layer

The SiH-B target has been irradiated from the side of thicker Si-H layer. The SiH-B+PR target may operate either in compression mode, when the laser pulse irradiates Si-H layer, or in protons increasing mode, when shooting on PR layer of the target. The protons accelerated from the Si-H substrate that propagate backward, against the laser-pulse propagation, are responsible for the nuclear reaction to occur.

Several numbers of targets were prepared in a matrix as shown in Figure 19, where each square represents a single target.

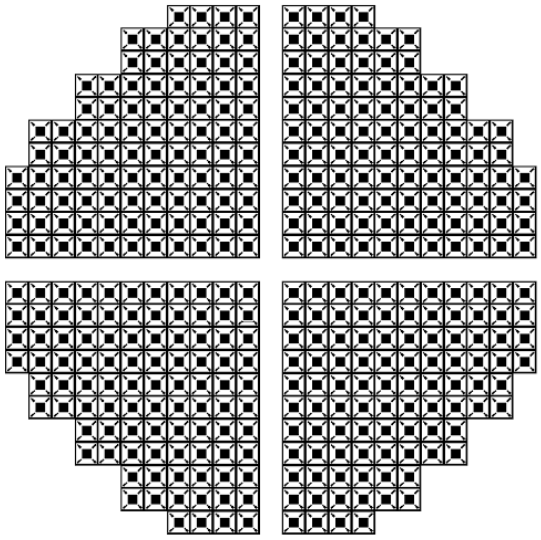

Figure 19: Scheme of the SiH-B target (black square) matrix

A picture of SiH-B + PR from both sides of the target is shown in Figure 20. The picture of SiH-B target is not present, since the top layer of the target is very reflective and the separation between each target is not visible.

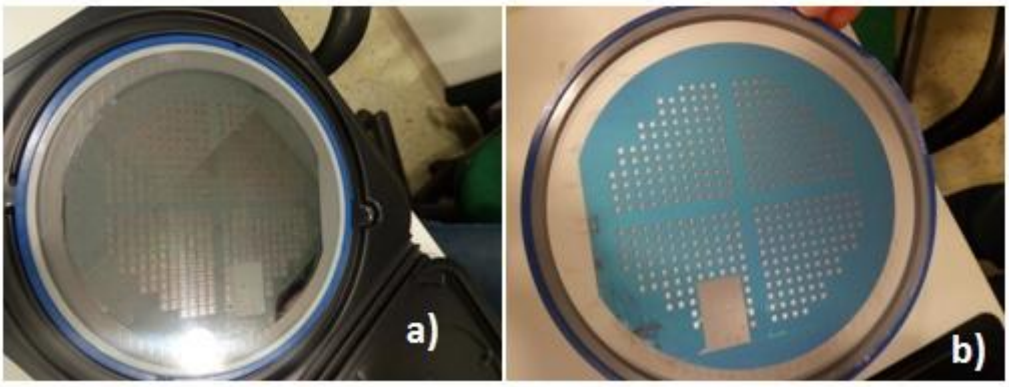

Figure 20: Picture of the SiH-B + PR target: a) from the PR side b) from the Si side

3.3. Detectors

As it was mentioned above, different kind radiation detectors were used in order to characterize the accelerated beam and the alpha particles produced in the fusion reaction in terms of energy, fluence and angular distribution.

TOF detectors

For the TOF measurement SiC and diamond detectors have been used. The detectors were placed at different angular positions with respect to the target normal. Since the interaction chamber geometry and the size (1m diameter sphere) did not allow to place the detectors at a sufficient long flight path to measure the temporal evolution signal of the particles with a reasonable temporal dynamics and time resolution, the TOF detectors were placed in about 1 m long pipes attached to the vacuum chamber, see Figure 21. In such way, the detectors were mounted with flight paths ranging between 90 cm and 160 cm as reported in Table 4.

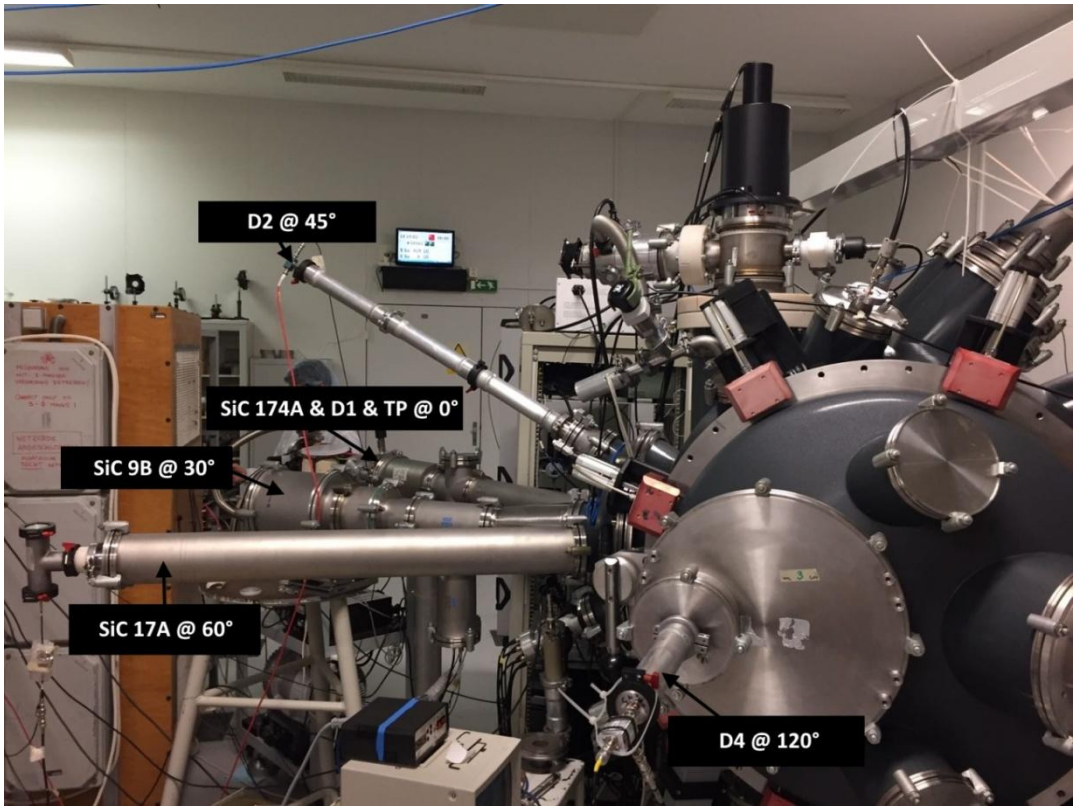

Figure 21: Picture of experimental setup mounted on interaction chamber. TOF pipes and TP are visible.

In order to eliminate the contribution of the low-energetic components of the accelerated beam, 6.5 µm and 10 µm Al filters were placed in front of the detectors. These filters stop proton and alpha particles with energies lower than a given cut-off energy which has been estimated using the energy loss program available in LISE++ code [43]. These values are listed in Table 3.

Table 3: Table of cut-off energies for two different filters placed before the detector

Al filter thickness	Proton cut-off energy	Alpha cut-off energy
6.5 μm	0.56 MeV	1.88 MeV
10 μm	0.77 MeV	2.75 MeV

The signal was obtained using fast digital oscilloscopes, between 600 MHz and 2 GHz bandwidth and 5 Gs/s and 10 Gs/s, placed in the experimental room shielded from the electromagnetic pulse using Faraday cage. To provide bias to each detector and to read-out the generated signal, RC circuits were used (typical values of RC are 100 MΩ and 1 nF). Angle and distance with respect to the target and voltage applied for each TOF detector are reported in Table 4.

Table 4: Angle position with respect to the target normal, distance from the target and applied voltage of each detector are listed. For D2 and SiC 17A detectors, the distance was changed during the experiment.

Detector	Angle	Distance	Bias
D1	0°	158.5 cm	+ 60 V
D2	45°	105 cm/139.1 cm	−100 V
D4	120°	108 cm	−100 V
SiC 174A	0°	158.5 cm	−300 V
SiC 9B	30°	136 cm	−300 V
SiC 17A	60°	140.5 cm/90.5 cm	−300 V

CR-39 detectors

CR-39 detectors belong to the group of solid state nuclear track detectors widely used for the charged particles detection and, particularly, for absolute dosimetry. It is made of polyallyl diglycol carbonate $C_{12}H_{18}O_7$. When the ionizing radiation impinges on the polymer structure of the detector it leaves a tail of broken chemical bonds within its path. Using a concentrated alkali solution (such as sodium hydroxide), its structure is attacked and left broken as the bulk of the plastic is etched away. However, the bond

along the path of charged particle has been already damaged, so chemical agent attacks this part more rapidly than it does in the bulk, revealing the tracks of the impinging particles. The size and the shape of these tracks are investigated using a microscope providing us the information about number of incoming particles according to a detector calibration CR-39 can also provide information about impinging particle mass, charge and energy. The size of the track is directly related to the energy released by the radiation in the CR-39. The track size measurement depends on the etching time, therefore, the longer etching time is the bigger is the observed diameter track allowing to obtain a higher resolution in the diameter size measurement which imply a better resolution in the energy estimation [44].

During the experiment, several CR-39s were placed inside the vacuum chamber to measure the alpha particle angular distribution and compare it with TOF measurement. In particular, each detector is dived into 4 quadrants covered by Aluminium foil of different thicknesses: 6, 10, 12 and 15 μm, see Figure 22, used to stop the low-energy protons accelerated from the target, allowing disentangling alphas from those protons, and to stop also alpha particles with different incident energy according to the filter thicknesses, allowing the measurement of the energy spectrum of the alpha particles impinging on the CR-39 using the differential absorbers and also to reduce the energy of high-energetic particles that are then completely stopped within the CR-39 material and can be analyzed. After each shot, CR-39 detector had to be removed in order not to reach the counting saturation limit (about $10^5/cm^2$) and to obtain the most accurate counting of the track number.

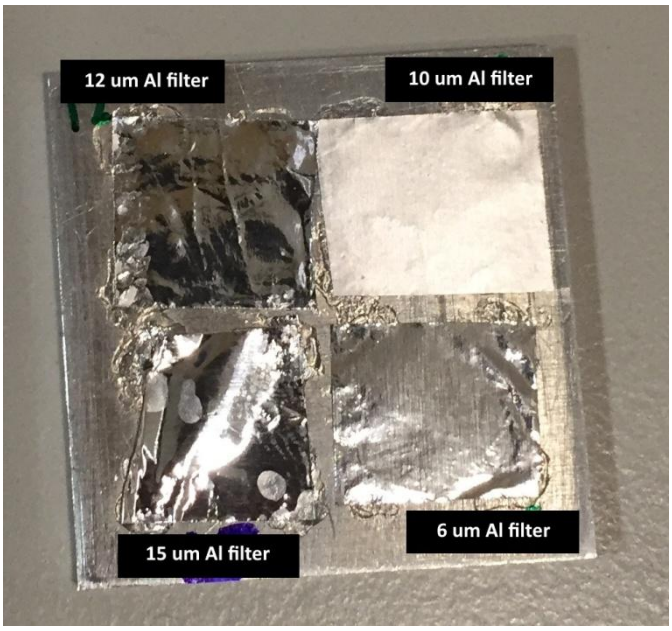

Figure 22: Picture of CR-39 detector, divided into 4 quadrants each with different thickness Al filter

Thompson parabola (TP) spectrometer

TP spectrometer is very often used method in laser-plasma experiments due to its capability to discriminate ions with different charge-to-mass ratio resulting in energy-resolved ion spectrum. This device uses the combination of electrostatic and magnetic fields parallel to each other applied transversely to the beam axis. According to the Lorentz Force that affects the particles due to the presence of the applied fields, the particle is deviated from its incident direction. Given particle follows the parabolic trajectory in the signal detected by Multi channel plates (MPC) or Image plates (IP) according to their charge-to-mass ratio. For this reason, TP spectrometer offers the possibility to identify different ions with the different charge states [45].

Two TP spectrometers were used during the experiment; one was placed at 0° with respect to the target normal in forward direction along the same pipe as the SiC 174A and D1, see Figure 21 and one in backward direction inside the interaction chamber.

3.4. Time-of-Flight Analysis

As it was mentioned before, the beam characterization by SiC and diamond detectors will be performed by using TOF configuration. The time-dependent ion current is measured by the detector placed in a distance *L*. Obtained signal is known as the TOF spectrum. An example of typical TOF spectrum is shown in Figure 23.

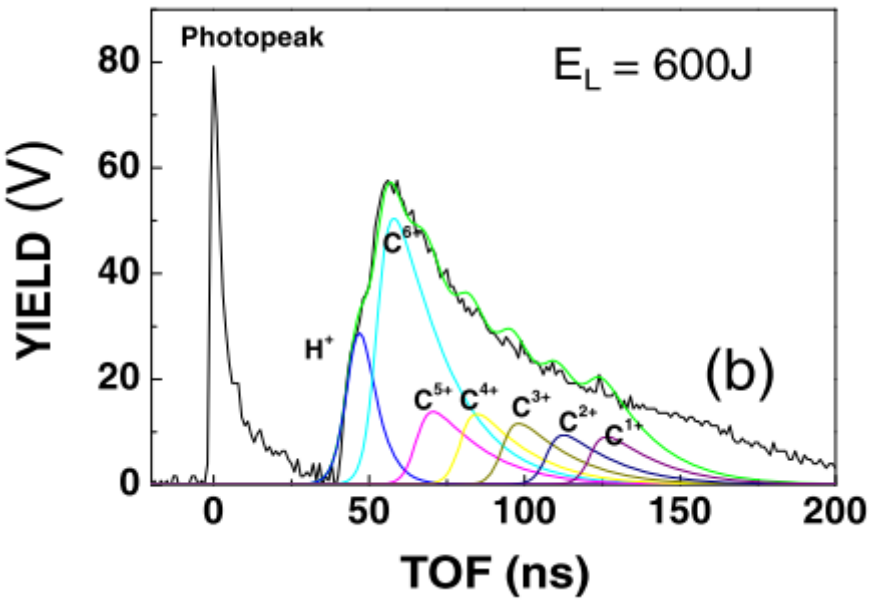

Figure 23: Typical TOF spectrum of particles from laser irradiation of polyethylene target during the experimented presented in [46]

Typically, a TOF signal consists of photopeak, generated by UV and X-ray laser-plasma radiation, followed by a tail of fast plasma electrons, a peak generated by the fastest proton group and a broad peak arising from the contribution of heavier ions with different charge, which are typically present in the target as contaminants. These particles are distributed in the TOF spectrum according to their kinetic energy, which depends on their mass, charge state and velocity.

The TOF analysis follows several crucial steps. In the first place, measured TOF needs to be calibrated according to the signal of photopeak by its displacement to zero time. In our calculations, we assume that the length of the laser pulse is much smaller than the sampling frequency of the oscilloscope. Therefore, we can say that all products of laser-

plasma interaction were created in the same time. Shifted TOF is then recalculated considering the time delay of the photons as follow:

$$t = TOF + \frac{L}{c} \tag{3.1}$$

where L is the flight path (the distance between the target and the detector), TOF is measured Time-of-Flight and c is the speed of light. The velocity of particle is then described as:

$$v = \frac{L}{t} = \frac{L}{TOF + \frac{L}{c}} \tag{3.2}$$

The kinetic energy of the particle is then expressed as:

$$E_k = \left(\frac{1}{\sqrt{1 - \frac{v^2}{c^2}}} - 1 \right) m_0 c^2 \tag{3.3}$$

This relativistic form of kinetic energy evaluation is used in case of measuring high-energy particles. The measured TOF signal provides information not just about the energy of impinging particles but also from the signal amplitude it is possible to extract their number thus allowing us to determine the flux and, hence, fluence of the particles and, as a result, the energy distribution of the laser-driven ion beams can be reconstructed.

According to the fact, that there is a difference in TOF for the different types of particles, their contributions in TOF spectrum have to be disentangled. The energy distribution of the single ion species ejected from the target can be observed by performing the fitting procedure based on the well-known Maxwell-Boltzmann (MB) shifted functions. This function describes the motion of the particles created by laser-plasma interaction. In particular, the TOF signal can be expressed as a sum of Gaussian functions, as proposed in [47], as follow:

$$F(L,t) = \frac{L^2}{TOF^5} \sum F_{i,0} \exp\left[-\frac{m_i}{2kT_i}\left(\frac{L}{TOF} - v_{s_i}\right)^2\right] \tag{3.4}$$

where $F_{i,0}$ is normalization constant, , k is the Boltzmann constant, T_i is the ion temperature m_i is the mass of the ion species constituting the partial current and v_{s_i} is the velocity of their centre-of-mass motion directed to the detector. Applying such procedure to a given group of ions enables us to determine their contribution in the TOF signal and then to convert its amplitude in number of particles taking into account the incident energy, energy loss in the detector and the detector response.

In order to reconstruct the number of impinging particles *N* of chosen energy *E* we assume its linear proportionality to the charge *Q* collected by detector's electrodes as follow:

$$Q = \frac{eNE}{E_G} \tag{3.5}$$

where *e* is the elementary charge, E_G is the minimal energy required for electron-hole pair inside the semiconductor and *E* is considered to be the kinetic energy of the particle that is released within the detector's sensitive layer. From the equation (3.5), the energy distribution can be obtained by providing its first derivative, as described in [48]:

$$\frac{\mathrm{d}N}{\mathrm{d}E} = \frac{E_G U(t)}{eRE^2}\left(\frac{1}{2}t + \delta t\right) \tag{3.6}$$

where $U(t)$ is the measured signal amplitude at a certain time *t* corresponding to investigated kinetic energy of the particles, *R* is the impedance of the detector's circuit including the oscilloscope termination, δt is the time step of the scope. Since the detectors can be placed in the different distance from the target as well as in the different angle with respect to target normal, it is necessary to characterize the energy distribution as a function of detector's solid angle $\Omega_{DETECTOR}$. The solid angle is defined as a ratio of the detector's area *S* to its distance from the target squared L^2. Therefore, the energy distribution can be expressed as:

$$\frac{\mathrm{d}N}{\mathrm{d}E\mathrm{d}\Omega} = \frac{E_G U(t) L^2}{eRE^2 S}\left(\frac{1}{2}t + \delta t\right) \tag{3.7}$$

However, in order to determine the real number of particles impinging the detector, the correct energy deposited in the detector must be evaluated. This evaluation was performed according to the energy loss of the particles within the filter placed before detector as well as the stopping power of the detector itself. The voltage applied to the detector determines the width of its sensitive layer therefore determine the cut-off energy of the particles completely stopped inside the detectors volume. For this reason, the simulation of the real deposited energy must have been performed.

4. Results

This chapter presents the results of the experiment described in previous chapters. A total of 2 reference shots with Al foil targets, 6 shots with SiHB targets and 6 shots with SiHB+PR targets have been analyzed; the data analysis and the interpretation of these results are object of this thesis. The analysis was performed using a program written using the MATLAB software based on the calculation described in section 3.4.

4.1. TOF analysis procedure

All of the TOF signals measured at a given distance were recalculated according to the photopeak position and correlated according to the offset due to the different cable lengths of the detector. In order to filter the particle signal from the electromagnetic noise, a smoothing, i.e. averaging procedure, of the TOF signal was performed using the moving average filter function of MATLAB. An example of the obtained TOF signal is shown in Figure 24.

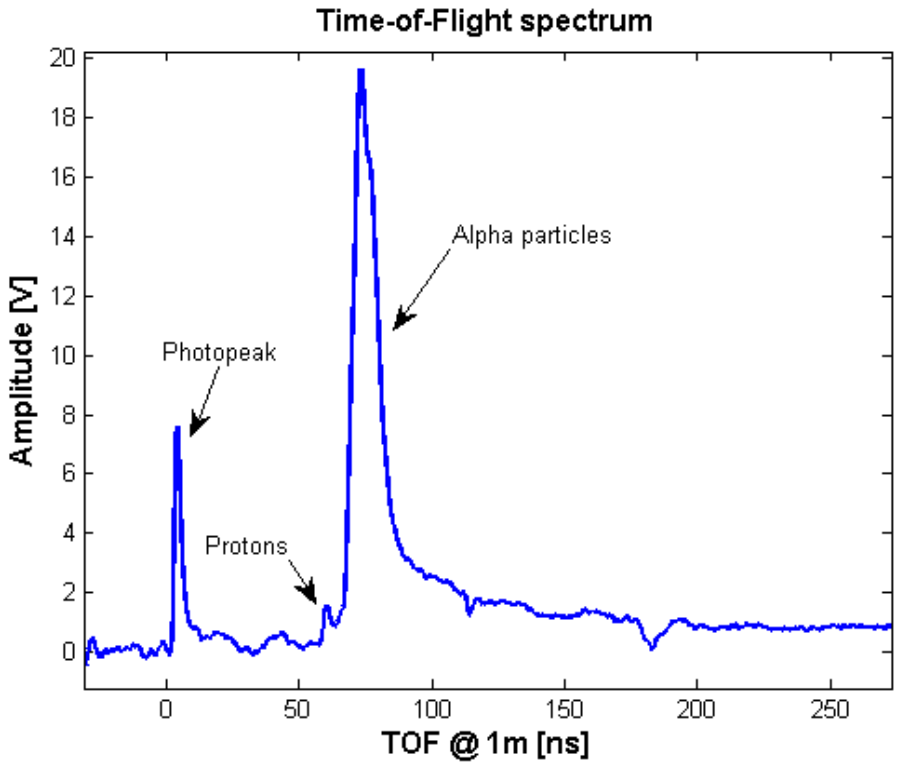

Figure 24: Typical TOF signal measured during the experiment. The position of the photopeak as well as proton and ion contributions is indicated

Slow ions heavier than protons and alpha particles have been stopped inside the Al filter placed in front of the detectors. Indeed, the filter thickness was also chosen to stop slow heavy ions accelerated from the target and their maximum energy has been measured thanks to the TP spectrometer for different charge states. Therefore, the TOF signal measured by the detectors is caused only by protons and alpha particles.

The TOF signal was then converted in the energy signal for both protons and alphas according to the equation (3.3). Figure 25 shows proton and alpha energy signals in the same picture. As one can see from this comparison, knowing the maximum energy of the proton accelerated from the target measured by the TP spectrometer at 0°, it is possible to indentify an energy region where the solely contribution to the signal is due to the alpha particles emitted by the proton-boron fusion reaction.

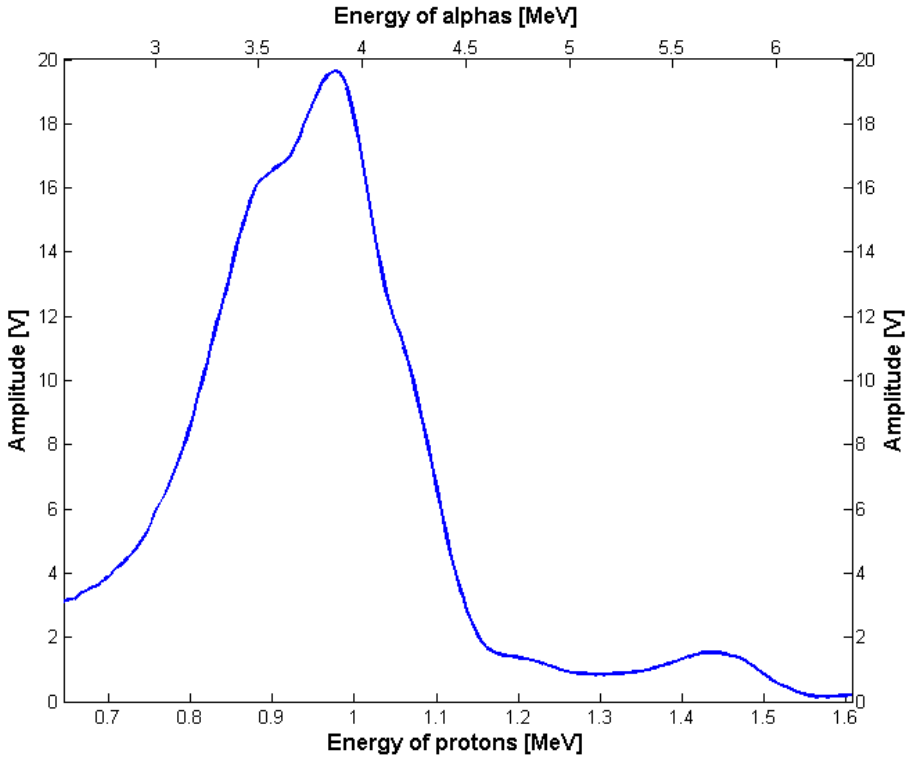

Figure 25: TOF spectrum recalculated to the energie of protons and alpha particles

As explained in chapter 1, the alpha particles are expected to be emitted from the proton-boron fusion reaction in an energy interval from about 2 MeV up to 10 MeV. However, the TOF of such alpha particles is similar to the TOF of protons accelerated

in the laser-target interaction (typical energies of proton accelerated with the Asterix laser system can reach 3 MeV). For this reason, in order to disentangle between the proton and alpha contribution in the TOF signal and to evaluate the correct number of alpha particles emitted for each shot, it is necessary to characterize the proton beam accelerated from a reference target, as for instance the 6.5 µm Al foil, in terms of maximum energies and energy distribution at different angles.

4.2. Reference shot

In order to obtain the cut-off energy at the different angles, proton energy distribution have been extracted from the signal measured at different angles using the equation (3.7), where energy losses in the detector as well as in the Al filter have been taken into account. In Figure 26 one can see proton energy distribution measured by SiC detectors respectively, placed at 0°, 30° and 60°. From the proton energy distributions shown in Figure 26, the total number of protons accelerated per solid angle has been also calculated.

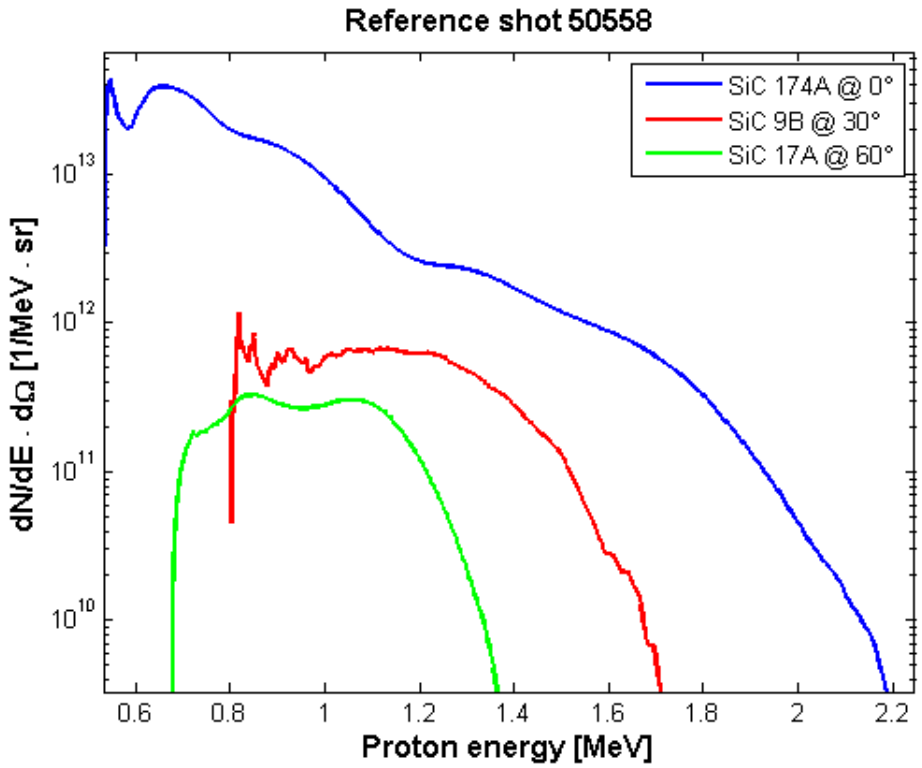

Figure 26: Proton energy distributions obtained at 0°, 30° and 60° for the 6.5µm Al target

In a TNSA like acceleration process, the protons with the highest energy, accelerated in the center of the electron sheath where the electric field is peaked, are emitted with small divergence. Going outside of the electron sheath center, the electric field is decreasing, resulting in lower energy protons emitted in a larger angular cone. As shown in Figure 26, the maximum proton energy measured decreases as the emission angle with respect to the target normal increases of about 20% per each 30°. Moreover, the number of particles decreases by approximately one order of magnitude per each 30°.

4.3. Targets doped with boron and hydrogen

A procedure similar to the one described above has been used for the analysis of the shots with SiH-B and SiH-B+PR targets. From the conversion of the TOF values in proton and alpha energies it is possible to identify the maximum energies of protons and alphas that can be present in the signal. Figure 27 and 28 show a comparison of the calculated proton and alpha energy spectra, respectively, for SiH-B and SiH-B+PR targets for all the detectors that could be analyzed, in particular detectors showing not saturated signal or showing a signal high enough that it could be discriminated from the electromagnetic noise contribution. The lowest particle energy detected is determined by the energy cut-off given by the Al filter placed in front of the detector.

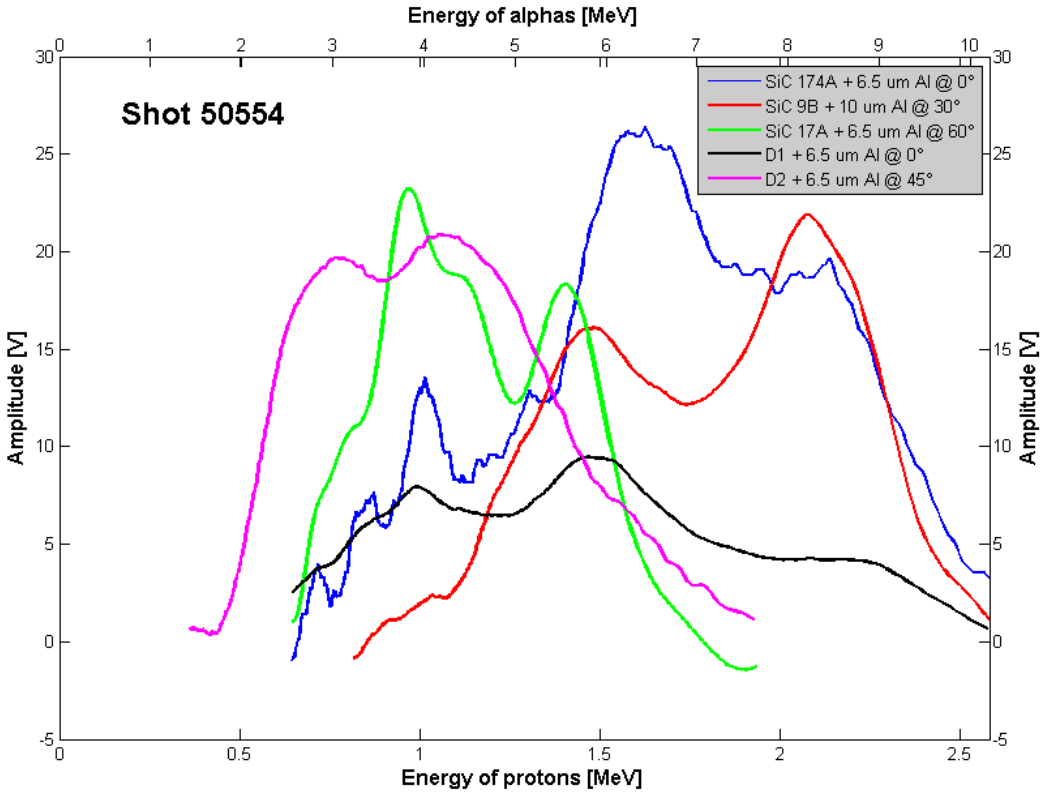

Figure 27: Comparison of the energy spectra corresponding to one shot with a SiH-B target for calculated both protons and alpha particles

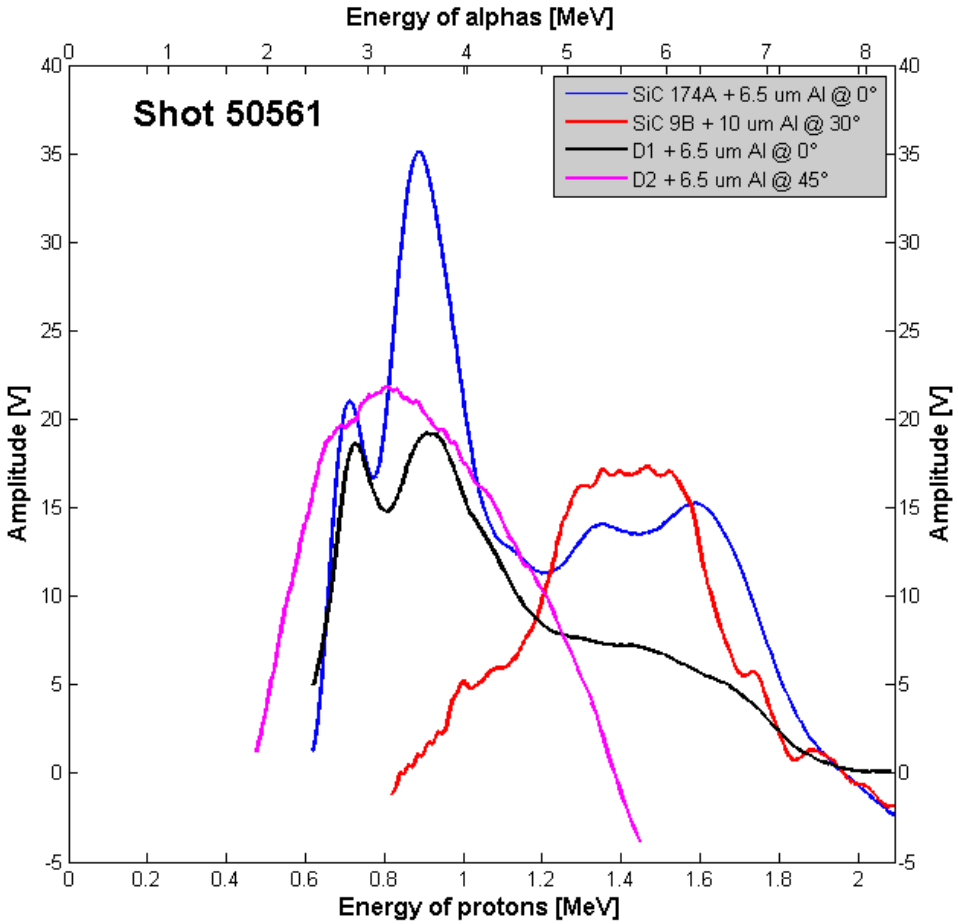

Figure 28: Comparison of the energy spectra corresponding to one shot with a SiH-B+PR target for calculated both protons and alpha particles

As one can see in Figure 27 and 28, for both boron doped targets there is a visible change in maximum proton energies measured by the detectors placed at larger angles, especially by for SiC 9B at 30°. The maximum energies detected with boron and hydrogen doped targets are higher than the ones observed in the reference shot and at larger angles, as for instance as 30°, reach the maximum proton energy measured at 0°. It is reasonable to assume that such increase in the maximum energy detected at larger angles can be ascribed to the contribution of alpha particles maximum energy reaching 8 MeV. This assumption is also supported by the fact that for proton energies corresponding to the highest cross section (675 keV) the angular distribution of the alpha particle emitted is uniform as suggested in [16].

Since protons accelerated from the target and alpha particles produced in this reaction have similar TOF, their TOF signals overlap. For this reason, in order to evaluate the number of alpha particles emitted with high accuracy an energy region where the signal can be generated solely by the impinging alpha particles has been identified. Taking into account the shift of the maximum proton energy observed as the detecting angle increases with both the reference target and with the boron doped targets, the alpha energy spectra have been analyzed considering an alpha energy threshold of 5 MeV. Therefore, the total number of alpha particles per steradiants has been extracted only for alpha particles with energies higher than 5 MeV. Such alpha energy corresponds to approximately 1.3 MeV proton energy, this value has been chosen as a compromise between the shift in the maximum proton energy with the emission angle and the alpha particle energy which could be generated in the proton-boron reaction. The alpha particle energy distributions corresponding to the energy signal shown in Figure 29 for SiH-B target and in Figure 30 for SiH-B+PR target together with the indication of the region where the distribution have been integrated.

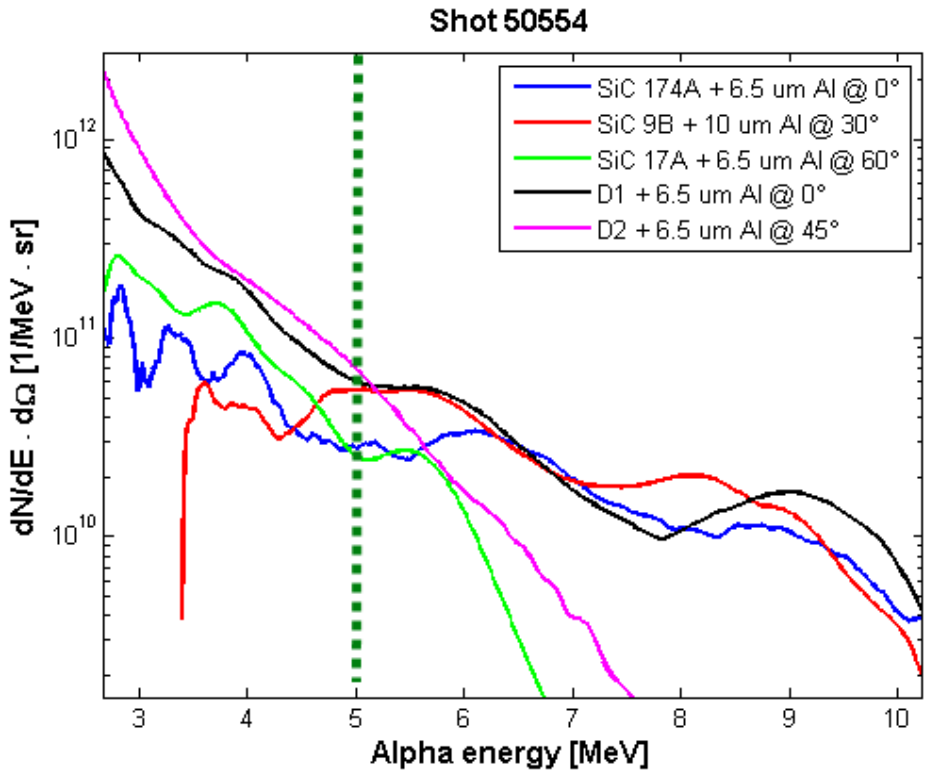

Figure 29: Alpha particles energy distributions extracted for the shot 50554 with SiH-B target

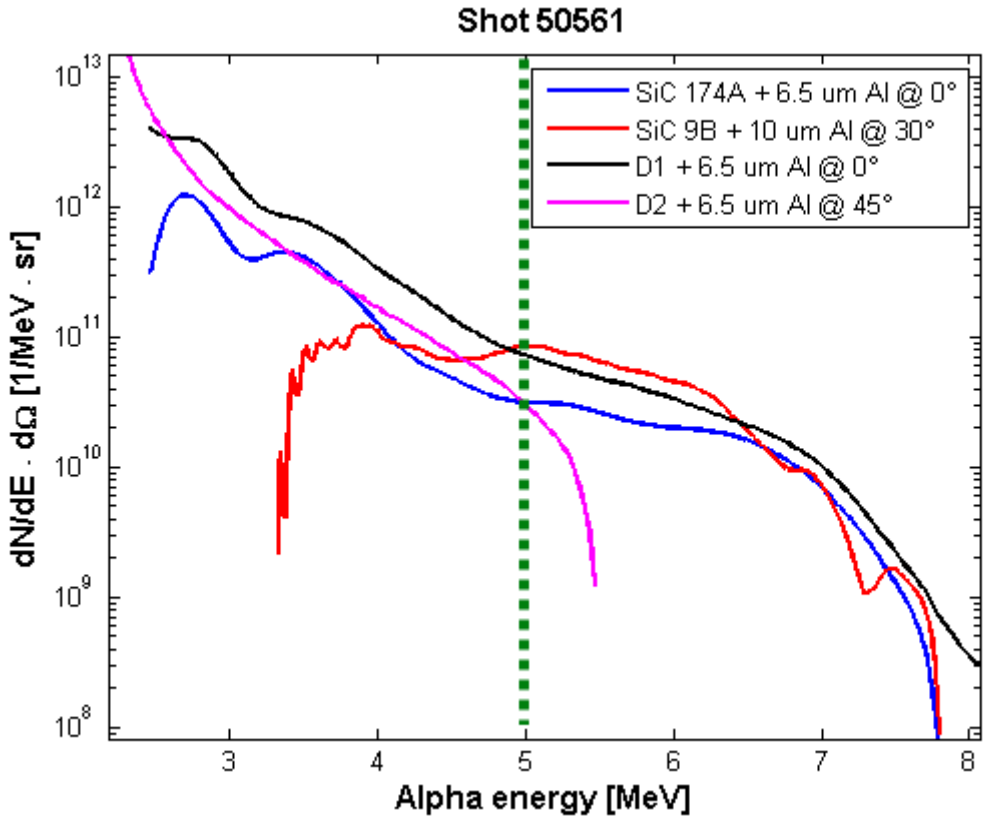

Figure 30: Alpha particles energy distributions extracted for the shot 50561 with SiH-B+PR target

For the alpha particle energy distribution of all shots see Appendix A and Appendix B for the results of shots with SiH-B target and SiH-B+PR target, respectively.

Since the maximum proton energies measured at 0° with both targets are similar to the ones measured with the reference target and to the ones measured by the TP spectrometer at 0° and since typically the highest number of protons is accelerated in the target normal direction, the alpha energy distribution for detectors placed at 0° were not analyzed and integrated since in this direction the main contribution is expected to be due to the proton signal and thus, the signal was converted to the number of protons for both targets, see Tables 5 and 6. The uncertainty has been calculated by error propagation formula applied to equation (3.7) resulting in mean error of approximately 25%.

Table 5: Number of protons detected at 0° for SiH-B targets together with the maximum observed energy and statistical error

Shot	Detector	Max proton energy [MeV]	Number of protons [particles/sr]	Error [particles/sr]
50548	SiC @ 0°	2.3	6.16e+12	±7.70e+11
50553	D1 @ 0°	2.6	3.22e+13	±4.03e+12
50559	SiC @ 0°	1.57	1.47e+12	±1.84e+11
	D1 @ 0°	1.51	1. 51e+13	±1.89e+12
50554	SiC @ 0°	2.6	2.61e+12	±3.26e+11
	D1 @ 0°	2.55	1.88e+13	±2.35e+12
50556	SiC @ 0°	1.94	4.99e+12	±6.23e+11
50560	SiC @ 0°	1.83	2.21e+12	±2.76e+11
	D1 @ 0°	1.92	9.70e+12	±1.21e+12

Table 6: Number of protons detected at 0° for SiH-B targets together with the maximum observed energy and statistical error

Shot	Detector	Max proton energy [MeV]	Number of protons [particles/sr]	Error [particles/sr]
50562	SiC @ 0°	1.8	3.66e+13	±4.57e+12
50564	SiC @ 0°	1.9	7.93e+12	±9.91e+11
50566	SiC @ 0°	3.1	2.60e+13	±3.25e+12
50567	SiC @ 0°	2.2	1.92e+13	±2.40e+12
50565	SiC @ 0°	2.3	1.46e+13	±1.83e+12
50563	SiC @ 0°	1.2	3.11e+12	±3.88e+11
	D1 @ 0°	1.3	6.82e+12	±8.53e+11
50561	SiC @ 0°	1.9	9.41e+12	±1.18e+12
	D1 @ 0°	1.9	4.01e+13	±5.01e+12

4.3.1. Number of alpha particles with SiH-B target

The number of alpha particles per solid angle has been extracted by integrating the alpha energy distribution for energies above 5 MeV for each detector at 30°, 45° and 60°. These values, together with the maximum alpha energy detected and the laser energy delivered to the target, are shown in Table 7. These numbers are also plotted in Figure 31 to show the angular distribution behavior of these alpha particles.

Table 7: Number of detected alpha particles for each detector at 30°, 45° and 60° for every shot with SiH-B target

Shot	Laser energy [J]	Detector	Max α energy [MeV]	Number of α particles [particles/sr]	Error [particles/sr]
50548	568	SiC @ 30°	6.1	5.29e+11	±6.61e+10
		SiC @ 60°	5.8	4.05e+10	±5.06e+9
		D2 @ 45°	5.6	1.11e+11	±1.38e+10
50553	607	SiC @ 30°	10.3	6.27e+11	±7.83e+10
		SiC @ 60°	9.5	2.16e+11	±2.70e+10
		D2 @ 45°	10.2	4.43e+11	±5.54e+10
50559	648	SiC @ 30°	6.7	3.13e+10	±3.91e+9
		D2 @ 45°	5.6	8.25e+10	±1.03e+10
50554	623	SiC @ 30°	10.2	3.86e+11	±4.83e+10
		SiC @ 60°	7.0	1.51e+11	±1.89e+10
		D2 @ 45°	7.4	3.52e+11	±4.40e+10
50556	614	SiC @ 30°	5.6	1.00e+11	±1.25e+10
		SiC @ 60°	5.2	3.54e+9	±4.43e+8
		D2 @ 45°	5.2	5.90e+10	±7.37e+9
50560	636	SiC @ 30°	7.5	2.44e+11	±3.05e+10
		SiC @ 60°	5.2	1.63e+10	±2.04e+9
		D2 @ 45°	5.3	2.66e+10	±3.33e+9

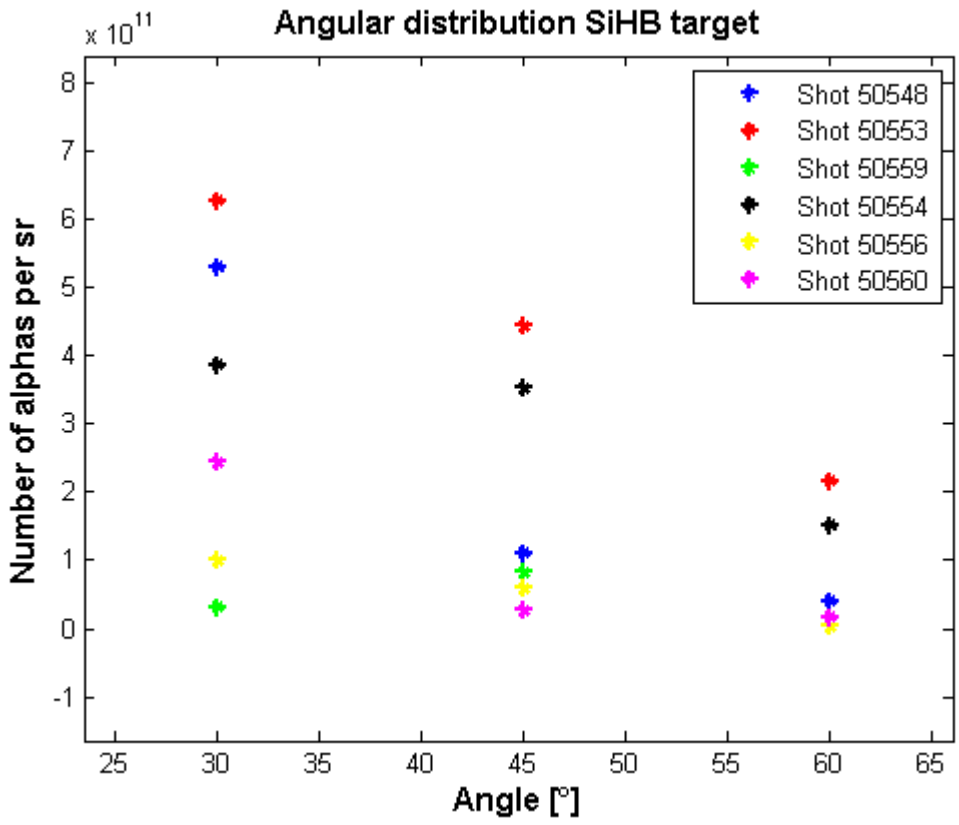

Figure 31: Number of alpha particles detected as a function of the emission angle from Table 7. Each shot in the figure is represented by a dot of the same color. Error bars are not included.

4.3.2. Number of alpha particles with SiH-B+PR target

In case of SiH-B+PR target, the compression mode was explored, i. e. the target was oriented in the way that laser was irradiating the Si-H side. The results of the analysis for this target are shown in Table 8 and they are also shown in Figure 32 in order to compare the number of alpha particles per steradiants for all the different shots.

Table 8: Number of detected alpha particles for each detector at 30°, 45° and 60° for every shot with SiH-B+PR target

Shot	Laser energy [J]	Detector	Max α energy [MeV]	Number of α particles [particles/sr]	Error [particles/sr]
50562	630	SiC @ 30°	5.5	6.88e+11	±8.60e+10
50564	622	SiC @ 30°	6.6	3.40e+11	±4.25e+10
		SiC @ 60°	5.5	5.19e+10	±6.48e+9
		D2 @ 45°	6.2	3.34e+11	±4.18e+10
50566	650	D4 @ 120°	6.1	2.76e+10	±3.45e+9
		D2 @ 45°	12.4	6.10e+11	±7.63e+10
50567	637	SiC @ 30°	8.2	6.48e+11	±8.1e+10
		SiC @ 60°	5.8	3.81e+10	±4.76e+9
		D2 @ 45°	7.2	5.20e+11	±6.50e+10
50565	679	SiC @ 60°	6.5	4.61e+11	±5.76e+10
		D @ 45°	7.0	5.50e+11	±6.88e+10
		D @ 120°	6.1	1.22e+11	±1.53e+10
50561	636	SiC2 @ 30°	7.3	5.17e+11	±6.46e+10
		D2 @ 45°	5.1	1.22e+11	±1.53e+10

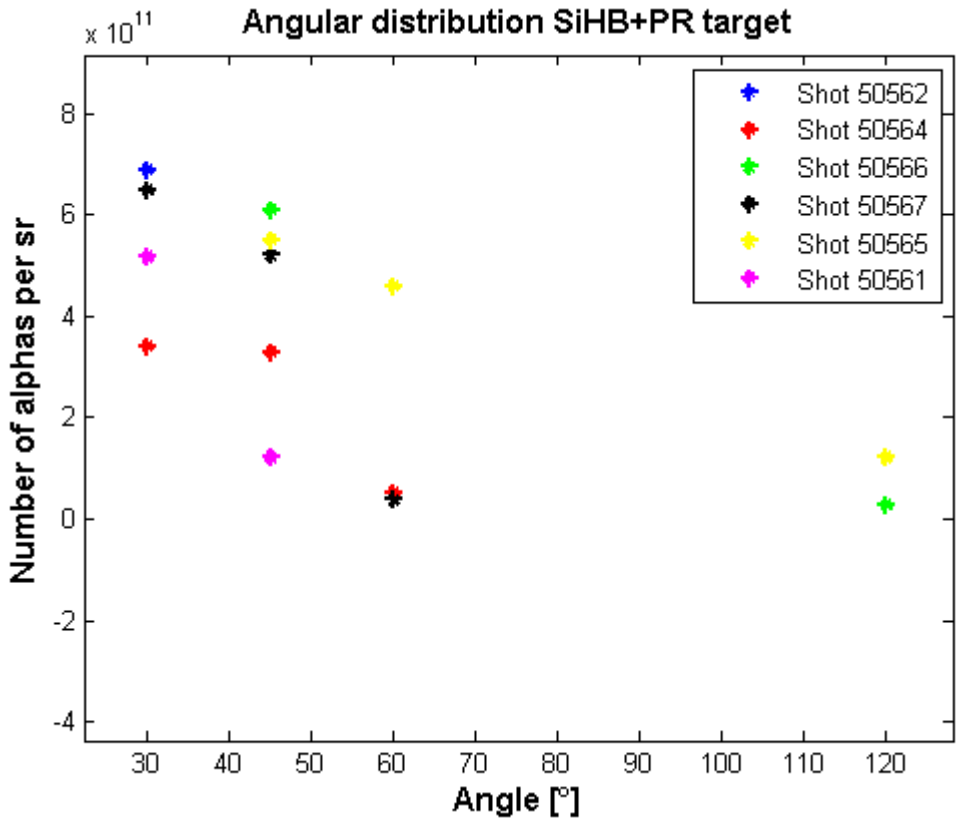

Figure 32: Number of alpha particles detected as a function of the emission angle from Table 8. Each shot in the figure is represented by a dot of the same color. Error bars are not included.

The SiH-B+PR target was also planned to be used also in a proton increasing mode, however, the experiment had to be interrupted due to the unexpected problems at the laser system and the second part of the experiment is currently on-going at PALS laboratory. This second part of experiment will allow increasing the statistics of the number of shots and confirming the preliminary results obtained as object of this thesis work. The results of the analysis will be discussed in the next chapter together with the preliminary results of CR-39 detectors.

5. Discussion

The data analysis showed an average alpha yield of about 10^{11} alpha particles per steradiants. The reasonably high number of protons from Tables 7 and 8 supports the possibility of production such high amount of alpha particles by triggering the proton-boron fusion. Compared to the results obtained by Picciotto et al. [35] an enhancement in the alpha particle yield of about two orders of magnitude has been observed. Moreover it has to be pointed out that the total number of alphas per solid angle unit extracted from the TOF signal correspond to a lower limit of the effective number of alpha particles emitted from the target, since the alpha particle energy distribution have been integrated for energies higher than 5 MeV while proton-boron reaction generates alpha particles also in a lower energy range.

In particular, the alpha yield obtained with the SiH-B target seems to show an exponential decrease with the emission angle. For the SiH-B+PR target the angular distribution seems to show a smoother slope indicating a more uniform emission than the SiH-B case with an increment in the alpha yield detected at 45° and 60° with respect the target without PR. This could be explained by the irradiation mode when the laser pulse was interacting with the silicon layer of the target. The PR layer might actually act as a “shield” compressing the plasma expansion and causing the particles to expand into the vacuum with higher divergence in comparison with the target without the PR layer.

As one can see in Figures 31 and 32, the range of number of alpha particles for both targets is pretty wide. The alpha yield from the proton-boron fusion reaction strongly depends on the number of protons accelerated by laser-plasma interaction in the energy range around 600 keV. However, this number depends on the laser energy and the focal position on the target thus this observed low shot-to-shot reproducibility was mainly due to the poor stability of these two factors.

Comparison with CR-39 results

The number of protons and alpha particles were obtained performing 1 hour etching of the detector in an alkali solution. After that, the traces with the same diameter,

corresponding to the same energy range, were counted. However, since most of the CR39 irradiated in the experiment were placed at about 30 cm from to the target, very few CR39s could be actually analyzed because almost all of them appeared already saturated after 1 hour etching procedure. The number of alpha particles was analyzed in the same energy region as the one selected for the TOF analysis in order to compare the results of the independent detectors. The preliminary results of the analysis are shown in Table 9.

Table 9: This table shows the number of alpha particles detected by CR-39 detectors for both hydrogen and boron doped Si target types

Shot	Target	Angle position [°]	Energy range [MeV]	Number of particles [particles/sr]
50556	SiH-B	90	5 – 5.5	1.37e+11
50562	SiH-B + PR	60	5 – 6.5	2.10e+11

The numbers of alpha particles detected by CR-39 detectors with the results of TOF analysis was compared. However, as mentioned before, most of the CR-39 detectors were mounted close to the target inside the interaction chamber at different angles with respect to the target normal than SiC and diamond detectors mounted on the long external pipes, therefore a comparison at the same angle between the results obtained with the two different kind of detectors was not always possible. As one can see from Table 9, the numbers of alpha particles detected by CR-39 detectors are rather in agreement within the same order of magnitude as the ones obtained in TOF measurement for the same energy region. Figures 33 and 34 show, respectively, a comparison between the angular distribution of alpha particles detected with TOF detectors for SiH-B and SiH-B + PR target together with the CR-39 result.

In order have a more clear comparison with the CR-39 results, the average number of alpha particles analyzed from TOF detectorat each angle has been calculated by averaging the results obtained for all the shots and plotted together with the uncertainty obtained by the standard deviation. As one can see in Figures 33 and 34, a rather good agreement can be observed between the number of particles detected by the CR-39 and the ones extracted from the TOF detectors.

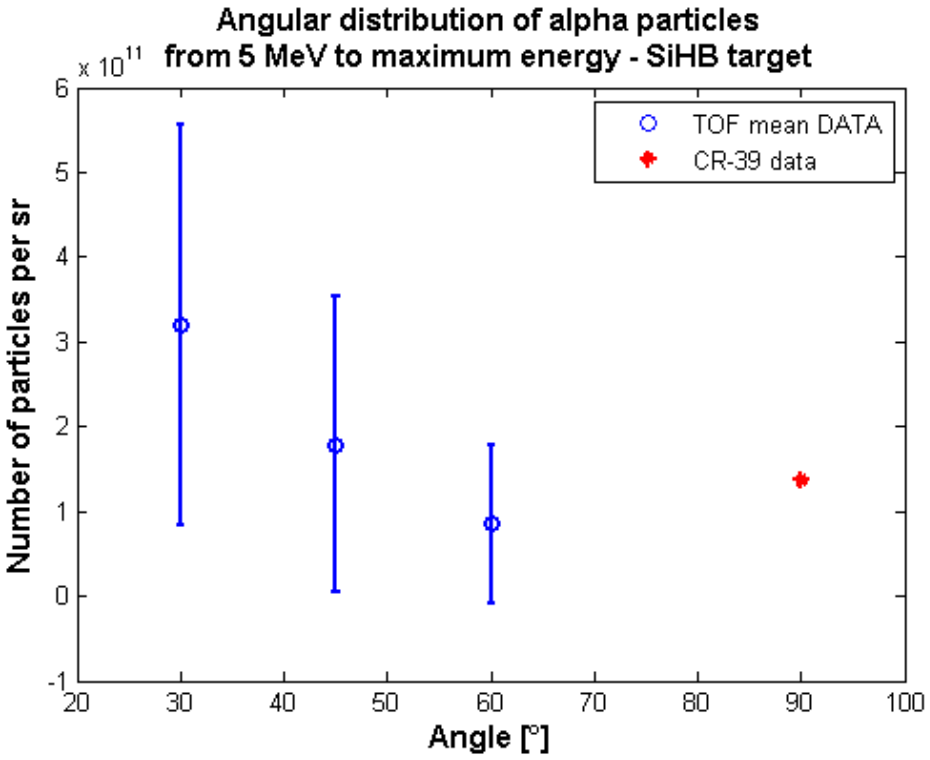

Figure 33: Average number of particles per steradiants evaluated by TOF analysis together with CR-39 results for the SiH-B target.

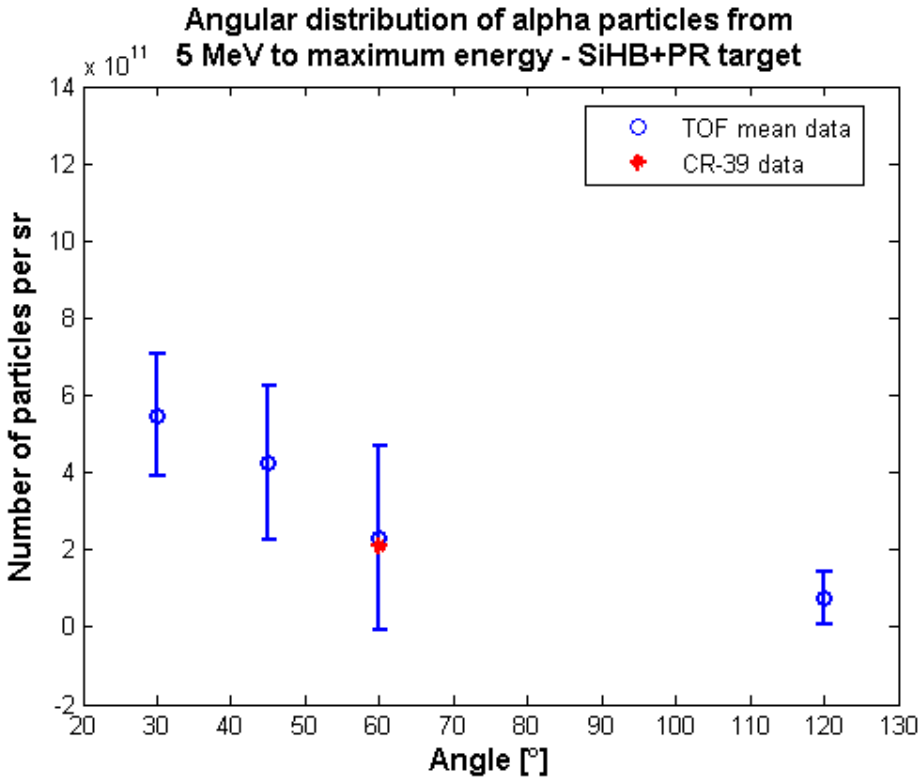

Figure 34: Averagenumber of particles per steradians evaluated by TOF analysis together with CR-39 results for theSiH-B+PR target.

Comparing the CR-39 results with the SiC detector placed at 60°, the number from CR-39 is well in agreement with the average number of particles detected by the TOF detector at this angle.

6. Conclusion

The main goal of this thesis was to investigate the products of laser-induced proton boron nuclear fusion with the use of specially developed Si targets doped with hydrogen and boron. The experiment was performed at PALS laser facility in Prague and was focused on the maximizing the number of alpha particles produced within this reaction, since in the previous experiment, this number was reaching 10^9 particles per steradian. This thesis deals with the analysis of the TOF detectors mounted inside the interaction chamber. The results have shown that the alpha particle yield has been increased by approximately two orders of magnitude in comparison with previous experiment reaching 10^{11} particles per steradian. This result was compared with the result of CR-39 detectors used during this experiment. The results of CR-39 analysis were coherent with the results of the TOF analysis implying that our preliminary assumption, that at larger detected angle the protons with energy higher than approximately 1.3 MeV are not present, was correct.

However, the number of particles per solid angle unit has been changing with every shot resulting in relatively high spread in number of particles in the alpha particles angular distribution. This is caused mainly due to the laser parameters like energy and focal position which affects the number of accelerated protons with energy with the highest cross section. Moreover, the number of shots with each target was not sufficient enough to conclude this thesis with the definite statement. For this reason, the next session of experiment is ongoing at the same laser facility in order to confirm these results.

7. References

[1] M. C. Kaluza, “Characterisation of Laser-Accelerated Proton Beams”, Max-Planck-Institut fur Quantenoptik, 2004.

[2] V. Scuderi et al., “Time of Flight based diagnostics for high energy laser driven ion beams”, *Journal of Instrumentation*, vol. 12, no. 03, pp. C03086-C03086, Mar. 2017.

[3] D. Schardt, T. Elsässer, and D. Schulz-Ertner, “Heavy-ion tumor therapy: Physical and radiobiological benefits”, *Reviews of Modern Physics*, vol. 82, no. 1, pp. 383-425, 2010.

[4] G. F. Knoll, *Radiation detection and measurement*, 4th ed. Hoboken, N.J.: John Wiley, c2010.

[5] W. R. Leo, *Techniques for nuclear and particle physics experiments: a how-to approach*, 2nd rev. ed. New York: Springer, c1994.

[6] W.T. Chu, „Heavy ion radiotherapy Yesterday, today and tomorrow“, *Proceedings of 10th heavy ion charged particle therapy symposium International symposium on heavy ion radiotherapy and advanced technology,* (p. 155). Japan

[7] O. Desouky and G. Zhou, “Biophysical and radiobiological aspects of heavy charged particles”, *Journal of Taibah University for Science*, vol. 10, no. 2, pp. 187-194, 2016.

[8] Wroe, “Immobilization Considerations for Proton Radiation Therapy”, *Technology in Cancer Research and Treatment*, p. -, 2013.

[9] U. Weber and G. Kraft, “Comparison of Carbon Ions Versus Protons”, *The Cancer Journal*, vol. 15, no. 4, pp. 325-332, 2009.

[10] D. -K. Yoon, J. -Y. Jung, and T. S. Suh, “Application of proton boron fusion reaction to radiation therapy: A Monte Carlo simulation study”, *Applied Physics Letters*, vol. 105, no. 22, p. 223507-, 2014.

[11] M. L. E. Oliphant and L. Rutherford, “Experiments on the Transmutation of Elements by Protons”, *Proceedings of the Royal Society A: Mathematical, Physical and Engineering Sciences*, vol. 141, no. 843, pp. 259-281, Jul. 1933.

[12] P. I. Dee and C. W. Gilbert, “The Disintegration of Boron into Three Formula-Particles”, *Proceedings of the Royal Society A: Mathematical, Physical and Engineering Sciences*, vol. 154, no. 881, pp. 279-296, Mar. 1936.

[13] C. Labaune, C. Baccou, V. Yahia, C. Neuville, and J. Rafelski, “Laser-initiated primary and secondary nuclear reactions in Boron-Nitride”, *Scientific Reports*, vol. 6, no. 1, p. -, 2016.

[14] R. E. Segel, S. S. Hanna, and R. G. Allas, “States in C 12 Between 16.4 and 19.6 MeV”, *Physical Review*, vol. 139, no. 4B, pp. B818-B830, 1965.

[15] W. M. Nevins and R. Swain, “The thermonuclear fusion rate coefficient for p- 11 B reactions”, *Nuclear Fusion*, vol. 40, no. 4, pp. 865-872, Apr. 2000.

[16] M. C. Spraker et al., “The 11B(p,α)8Be → α α and the 11B(α,α)11B Reactions at Energies Below 5.4 MeV”, *Journal of Fusion Energy*, vol. 31, no. 4, pp. 357-367, 2012.

[17] T. H. MAIMAN, “Stimulated Optical Radiation in Ruby”, *Nature*, vol. 187, no. 4736, pp. 493-494, 1960-8-6.

[18] G. A. Mourou, T. Tajima, and S. V. Bulanov, “Optics in the relativistic regime”, *Reviews of Modern Physics*, vol. 78, no. 2, pp. 309-371, 2006.

[19] T. Z. Esirkepov, S. V. Bulanov, C. Stehlé, C. Joblin, and L. d’Hendecourt, “Fundamental physics and relativistic laboratory astrophysics with extreme power lasers”, *EAS Publications Series*, vol. 58, pp. 7-22, 2012.

[20] H. Daido, M. Nishiuchi, and A. S. Pirozhkov, “Review of laser-driven ion sources and their applications”, *Reports on Progress in Physics*, vol. 75, no. 5, p. 056401-, May 2012.

[21] D. Jung, “Ion acceleration from relativistic laser nano-target interaction”, Munchen, 2012.

[22] A. P. L. Robinson, M. Zepf, S. Kar, R. G. Evans, and C. Bellei, “Radiation pressure acceleration of thin foils with circularly polarized laser pulses”, *New Journal of Physics*, vol. 10, no. 1, p. 013021-, Jan. 2008.

[23]L. Yin, B. J. Albright, D. Jung, R. C. Shah, S. Palaniyappan, K. J. Bowers, A. Henig, J. C. Fernandez, and B. M. Hegelich, “Break-out afterburner ion acceleration in the longer laser pulse length regime”, *Physics of Plasmas*, vol. 18, no. 6, p. 063103-, 2011.

[24] Roth, M., & Schollmeier, M. (2016). „Ion Acceleration—Target Normal Sheath Acceleration“. *CERN Yellow Reports, 1*, 231.

[25] M. Gauthier, “Experimental Study of Ion Stopping Power in Warm Dense Matter: Charge-state Distribution Measurements of Ions Leaving Warm Dense Matter”, Ecole Polytechnique, 2013.

[26] A. Macchi, M. Borghesi, and M. Passoni, “Ion acceleration by superintense laser-plasma interaction”, *Reviews of Modern Physics*, vol. 85, no. 2, pp. 751-793, 2013.

[27] Y. Sentoku, T. E. Cowan, A. Kemp, and H. Ruhl, “High energy proton acceleration in interaction of short laser pulse with dense plasma target”, *Physics of Plasmas*, vol. 10, no. 5, pp. 2009-2015, 2003.

[28] B. M. Hegelich, “Acceleration of heavy Ions to MeV/nucleon Energies by Ultrahigh-Intensity Lasers”, Ludwig-Maximilians-Universität Munchen, 2002.

[29] http://static.sif.it/SIF/resources/public/files/va2011/borghesi_0624.pdf - cited 1.5.2017

[30] C. Obcemea, “Potential clinical impact of laser-accelerated beams in cancer ion therapy”, *Nuclear Instruments and Methods in Physics Research Section A: Accelerators, Spectrometers, Detectors and Associated Equipment*, vol. 829, pp. 149-152, 2016.

[31] https://www.eli-beams.eu/cs/

[32] F. Schillaci et al., “Design of a large acceptance, high efficiency energy selection system for the ELIMAIA beam-line”, *Journal of Instrumentation*, vol. 11, no. 08, pp. P08022-P08022, Aug. 2016.

[33] G. Milluzzo et al., “Laser-accelerated ion beam diagnostics with TOF detectors for the ELIMED beam line”, *Journal of Instrumentation*, vol. 12, no. 02, pp. C02025-C02025, Feb. 2017.

[34] D. Margarone et al., “Full characterization of laser-accelerated ion beams using Faraday cup, silicon carbide, and single-crystal diamond detectors”, *Journal of Applied Physics*, vol. 109, no. 10, p. 103302-, May 2011.

[35] A. Picciotto et al. “Boron-Proton Nuclear-Fusion Enhancement Induced in Boron-Doped Silicon Targets by Low-Contrast Pulsed Laser”, *Physical Review X*, vol. 4, no. 3, p. -, 2014.

[36] http://www.powerguru.org/semiconductor-doping/

[37] G. Bertuccio, D. Puglisi, L. Torrisi, and C. Lanzieri, “Silicon carbide detector for laser-generated plasma radiation”, *Applied Surface Science*, vol. 272, pp. 128-131, 2013.

[38] F. Nava et al., “Silicon carbide and its use as a radiation detector material”, *Measurement Science and Technology*, vol. 19, no. 10, p. 102001-, Oct. 2008.

[39] M. De Napoli, G. Raciti, E. Rapisarda, and C. Sfienti, “Light ions response of silicon carbide detectors”, *Nuclear Instruments and Methods in Physics Research Section A: Accelerators, Spectrometers, Detectors and Associated Equipment*, vol. 572, no. 2, pp. 831-838, 2007.

[40] M. Friedl, “Diamond Detectors for Ionizing Radiation”, University of Technology, Vienna, 1999.

[41] M. Marinelli et al. “Analysis of laser-generated plasma ionizing radiation by synthetic single crystal diamond detectors”, *Applied Surface Science*, vol. 272, pp. 104-108, 2013.

[42] http://www.pals.cas.cz/laser/

[43] http://lise.nscl.msu.edu/lise.html

[44] Z. Tayyeb, "Use of Cr-39 Polymer for Radiation Dosimetry", *Journal of King Abdulaziz University-Engineering Sciences*, vol. 22, no. 1, pp. 79-96, 2010.

[45] A. Alejo, D. Gwynne, D. Doria, H. Ahmed, D. C. Carroll, R. J. Clarke, D. Neely, G. G. Scott, M. Borghesi, and S. Kar, "Recent developments in the Thomson Parabola Spectrometer diagnostic for laser-driven multi-species ion sources", *Journal of Instrumentation*, vol. 11, no. 10, pp. C10005-C10005, Oct. 2016.

[46] P. Musumeci, M. Cutroneo, L. Torrisi, A. Velyhan, M. Zimbone, and L. Calcagno, "Silicon carbide detectors for diagnostics of ion emission from laser plasmas", *Physica Scripta*, vol. T161, p. 014021-, May 2014.

[47] J. Krása, "Gaussian energy distribution of fast ions emitted by laser-produced plasmas", *Applied Surface Science*, vol. 272, pp. 46-49, 2013.

[48] J. Prokůpek, "Diagnostic Systems for Laser-Accelerated Ion Beams", CZECH TECHNICAL UNIVERSITY IN PRAGUE, 2012.

8. Appendix

8.1. Appendix A

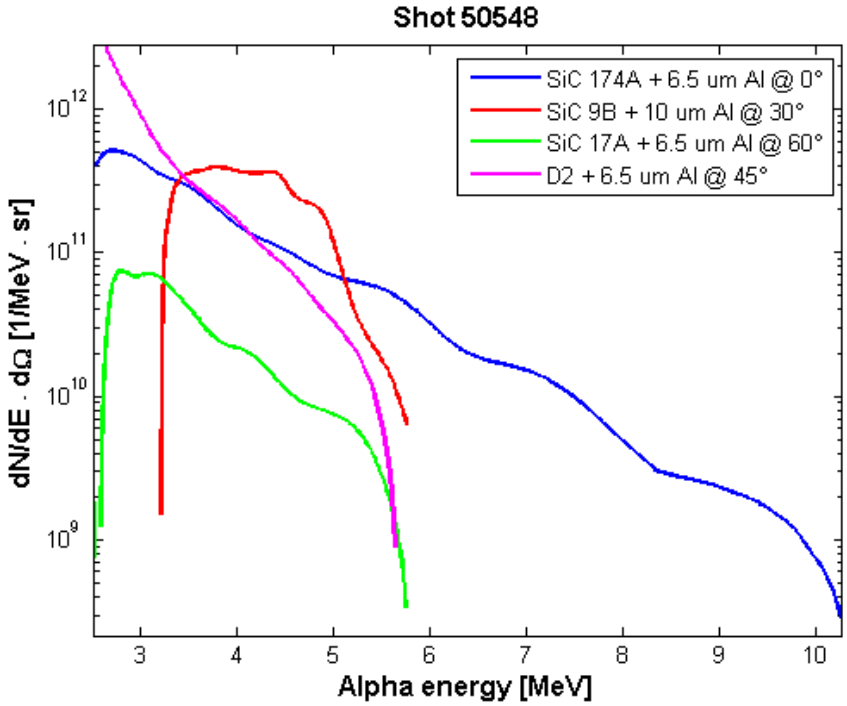

Figure 35: Alpha particles energy distributions extracted for the shot 50548

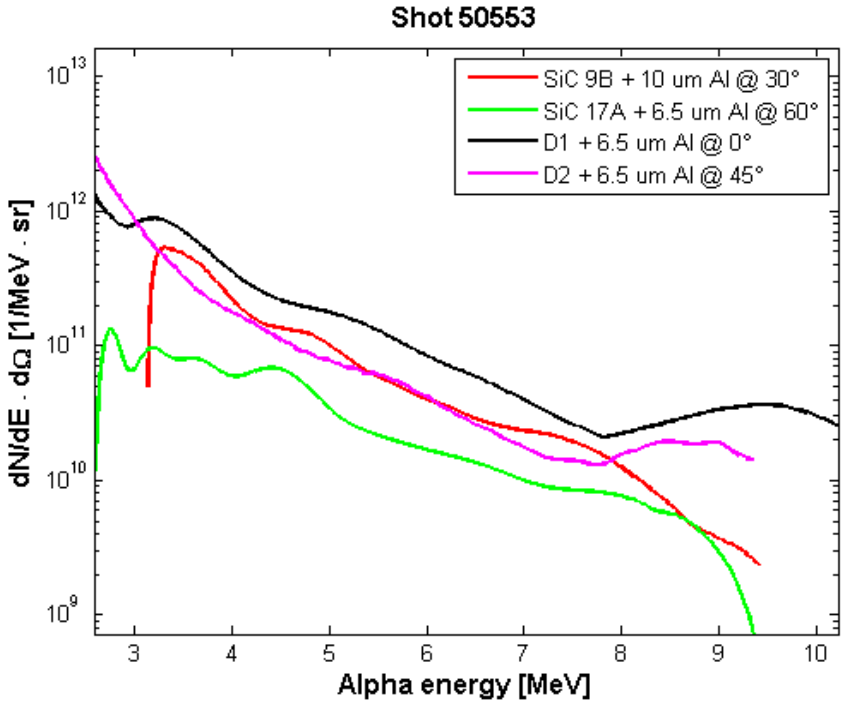

Figure 36: Alpha particles energy distributions extracted for the shot 50553

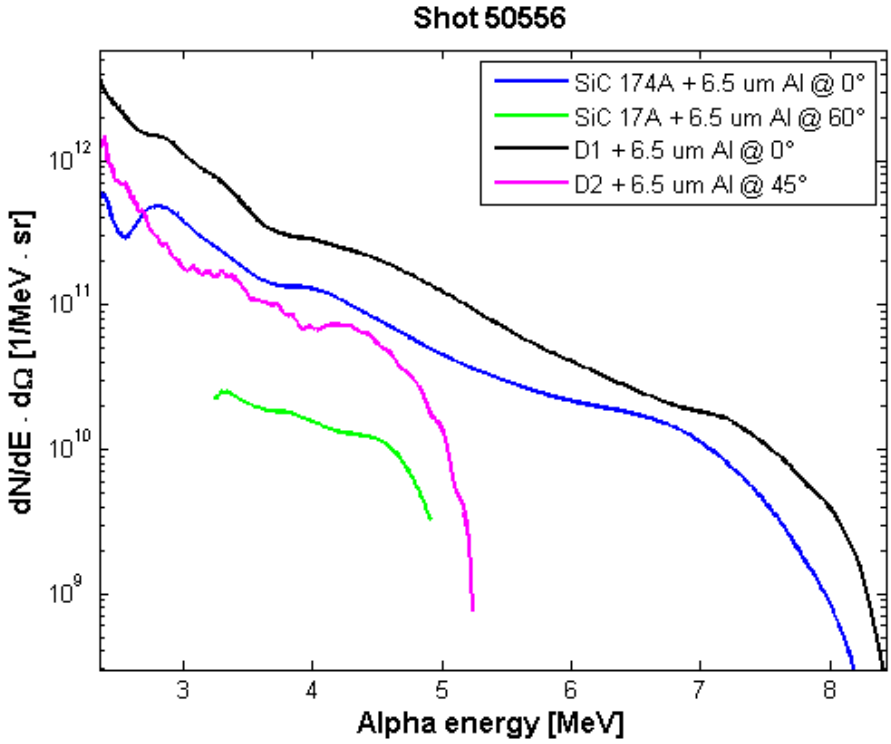

Figure 37: Alpha particles energy distributions extracted for the shot 50556

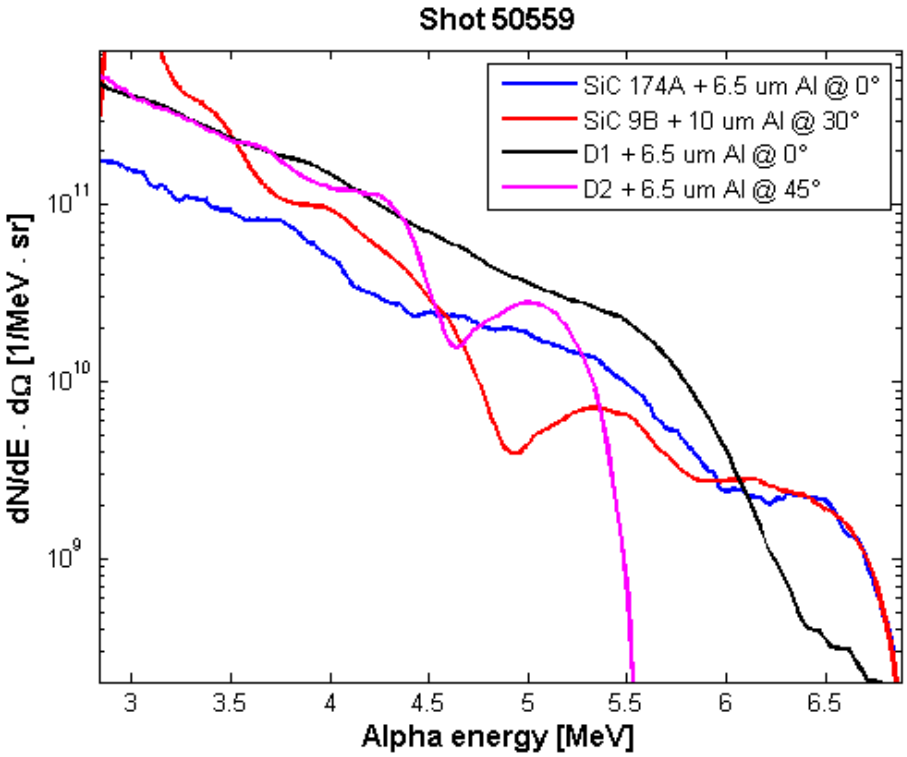

Figure 38: Alpha particles energy distributions extracted for the shot 50559

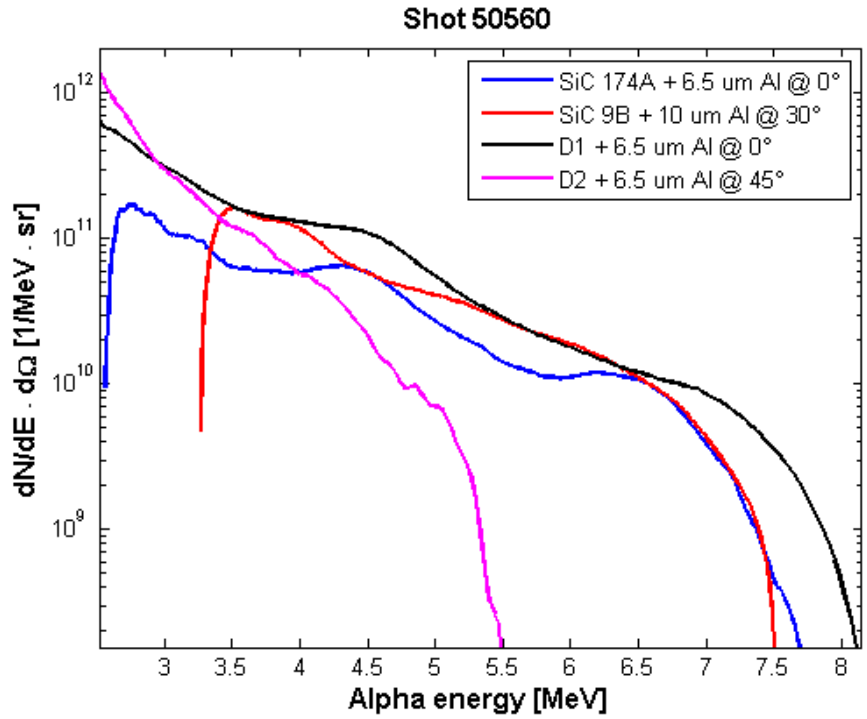

Figure 39: Alpha particles energy distributions extracted for the shot 50560

8.2. Appendix B

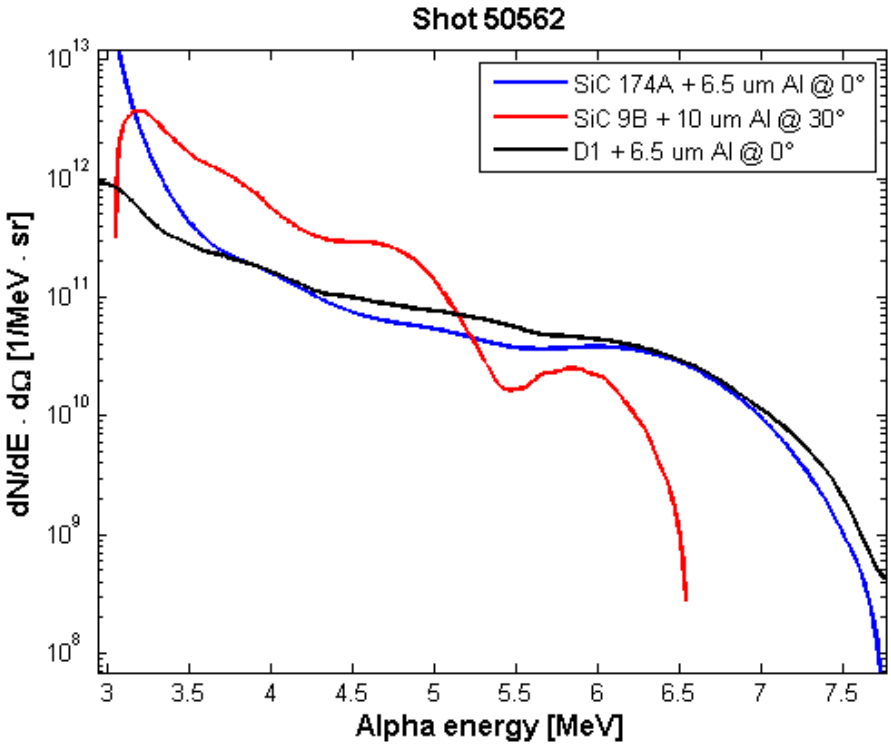

Figure 40: Alpha particles energy distributions extracted for the shot 50562

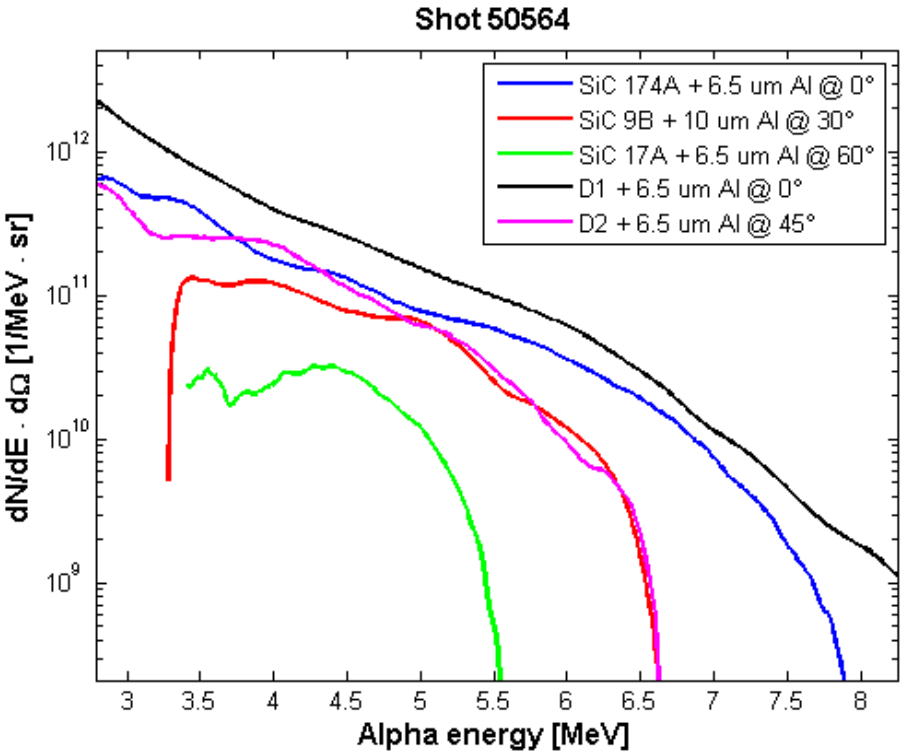

Figure 41: Alpha particles energy distributions extracted for the shot 50564

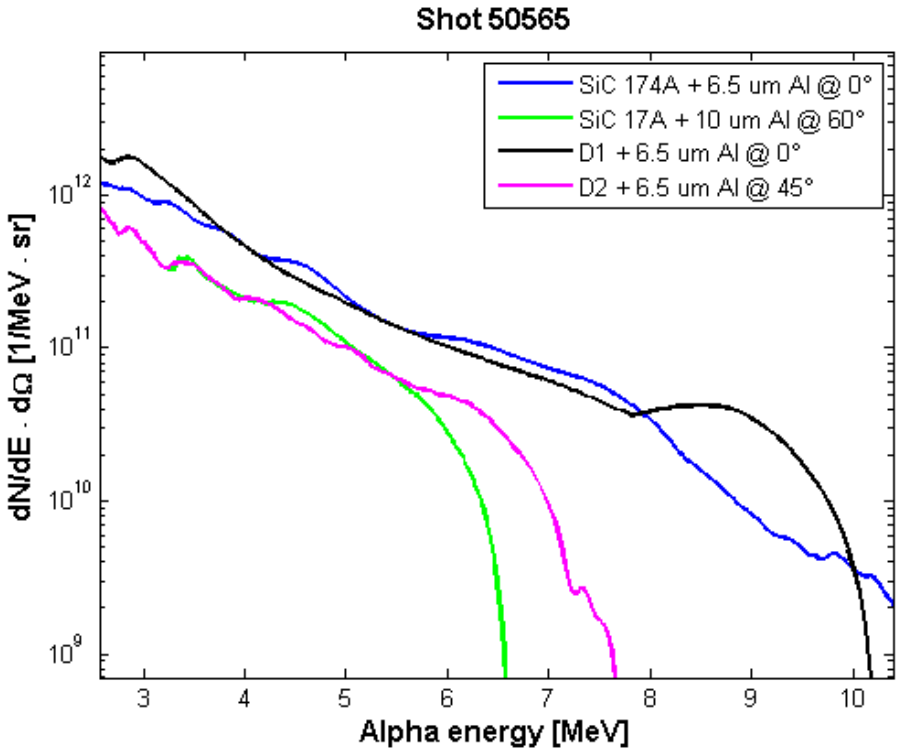

Figure 42: Alpha particles energy distributions extracted for the shot 50565

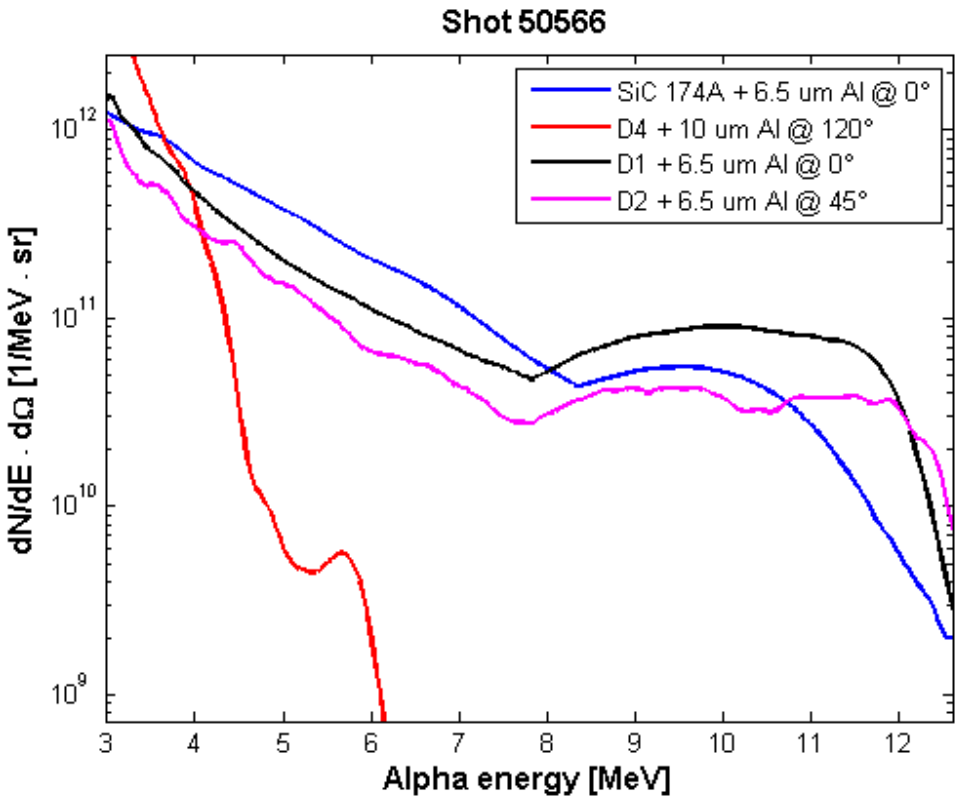

Figure 43: Alpha particles energy distributions extracted for the shot 50566

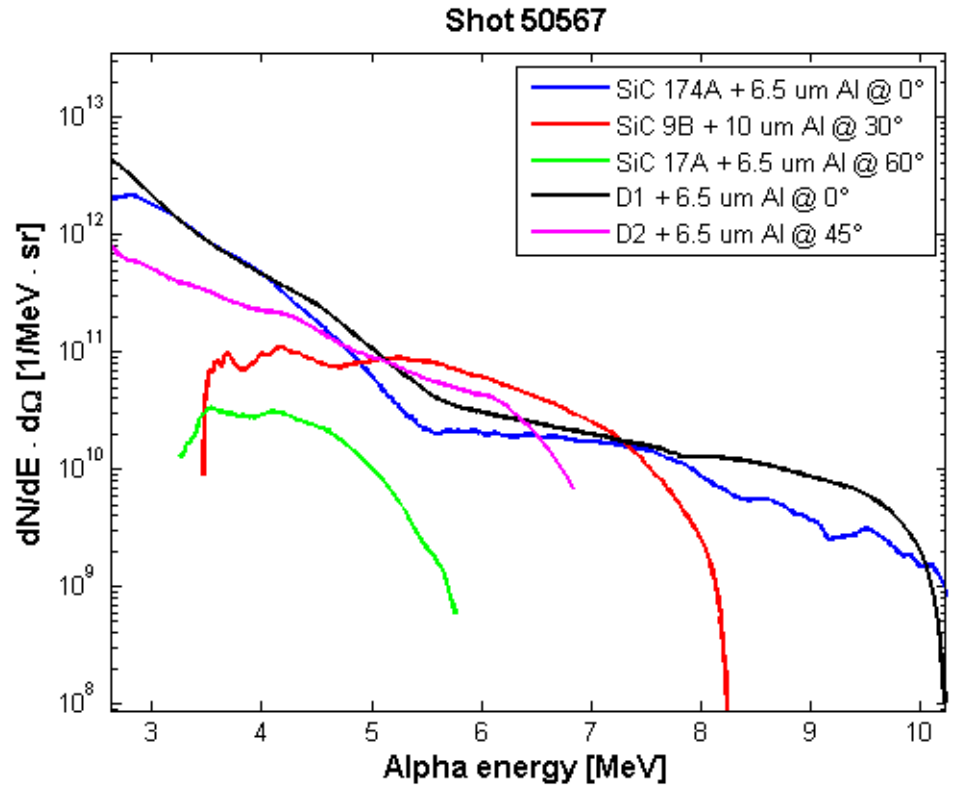

Figure 44: Alpha particles energy distributions extracted for the shot 50567